Representative Plasma Diagnostics: Representative Plasma Diagnostics in Magnetic Fusion Confinement Devices

Contents

1 Introduction

Most of the information within this report is derived and summarized from the following sources[1, 2, 3, 4], with paper references taken largely from those referred to within those books. It is suggested that one follow the table of contents in deciding which section to read; one should consult the references that refer to plasma diagnostics[1, 2, 3, 4], as well as the collection of conference proceedings, *Diagnostics for Experimental Thermonuclear Fusion Reactors*[5], if one wishes to understand a specific diagnostic in more detail. It is suggested that one reads chapters 1-8 separately and chapter 9, which describes a summary of plasma diagnostics in the Ignitor fusion reactor, as well as space and time resolutions of some diagnostics.

1.1 Background on Toroidally Confined Plasmas

During the past fifty years, the science of fusion, fusion plasma confinement, and hence fusion energy generation have undergone significant advances. An enormous amount of research, in Russia, the United States, Europe, and Japan, has gone towards understanding of magnetically confined toroidal plasmas towards the development of a future fusion reactor as well as towards the dynamics of magnetically confined plasmas.

All toroidal confinement devices require the existence of a toroidal and poloidal magnetic field to confine the plasma against otherwise substantial particle drifts. For instance, for plasma confined only by a toroidal magnetic field, magnetic curvature and ∇B drifts cause the electrons and ions to drift in opposite directions vertically. Charge separation between the electrons and ions results in a vertical electric field, resulting in a radial $\mathbf{E} \times \mathbf{B}$ drift of both electrons and ions.

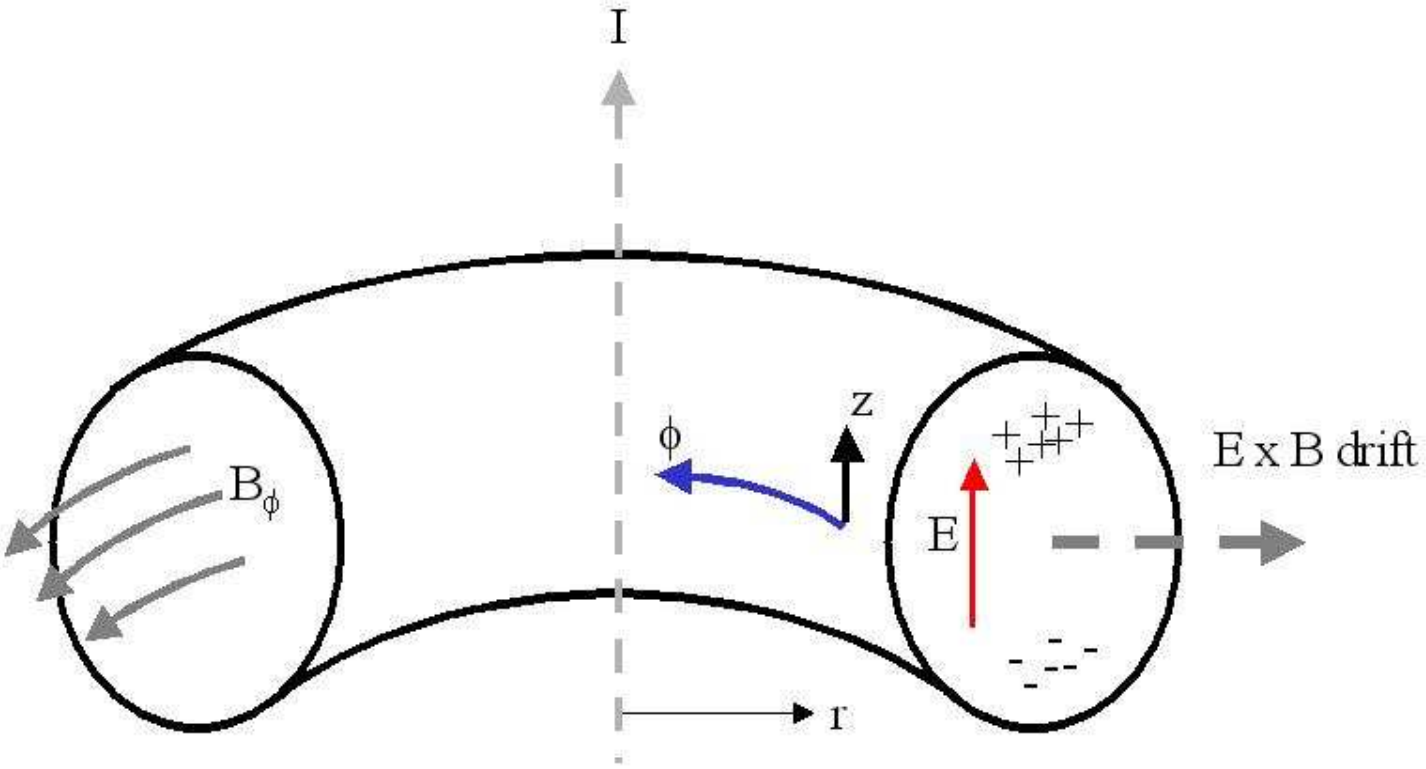

Figure 1.1: In a simple torus, magnetic curvature and ∇B drifts act on ions and electrons oppositely, resulting in charge separation. Depicted is the net external current that results in the $1/r$ profile of the toroidal magnetic field, and the directions of increasing toroidal angle ϕ, increasing z, and increasing r. For particles travelling along increasing ϕ, one gets the above charge separation, electric field, and outward $\mathbf{E} \times \mathbf{B}$ drift. The above figure is taken from [6].

Stellarators provide a poloidal field through external currents, while tokamaks produce poloidal fields through transformer-induced toroidal currents in the plasma. Furthermore, the existence of poloidal fields results in the shear of magnetic lines of force that suppress interchange, or gravitational, instabilities in the plasma. The plasma within a tokamak or stellarator may be heated through joule heating, RF heating at the electron cyclotron or ion cyclotron harmonics, or through the injection of neutral ions into the plasma.

The range of temperature and number density over which magnetically confined fusion plasmas occur is shown in the figure below, reproduced from the following reference[1]:

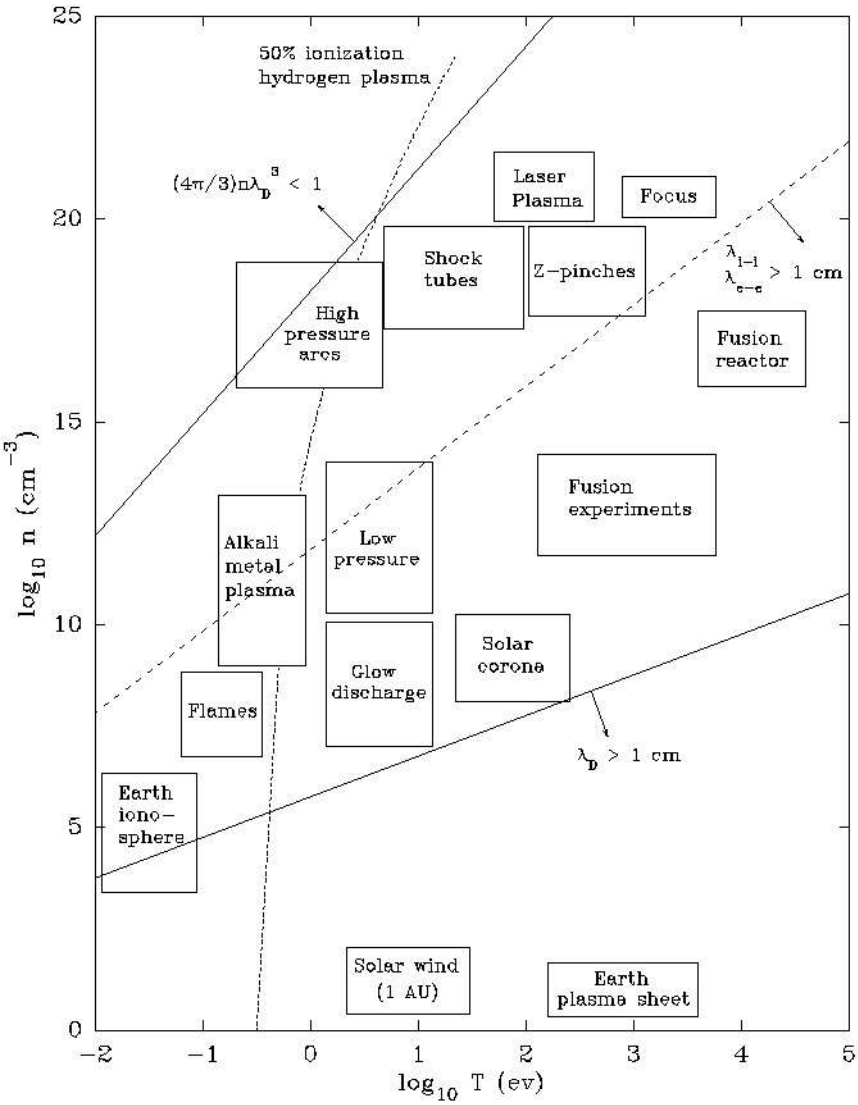

Figure 1.2: The approximate regimes of temperature and number density for various plasmas. The diagnostics described here apply to fusion experiment plasmas, with temperatures of $\sim 10^3$ eV and number densities of $10^{11} - 10^{14}$ cm^{-3}.

1.2 Background of the Report

This report will focus on the most important quasistationary plasma diagnostics for toroidal plasma confinement devices. Therefore, the following measurements of quasistationary parameters are described. Since I am detailing representative diagnostics within a tokamak plasma, which involves a mixture of theoretical concepts and measurements (for example, both neutron spectroscopy and interferometry use chord-averaged measurements which must be abel-inverted; electron cyclotron emission and visible bremsstrahlung both involve emission from free electrons), the organization of this report is given by the following:

1. magnetic measurements to determine quasiequilibrium toroidal and poloidal magnetic fields and global properties (toroidal current, toroidal voltage, plasma toroidal beta). A short introduction on electronic integration and differentiation is included.

2. A background on emission from nonrelativistic free electrons.

3. An introduction to Abel inversion. Abel inversion is used in the determination of field quantities when one has chord-averaged quantities.

4. Electron density/internal magnetic field measurements. Microwave reflectometry and two-color interferometry is used to measure chord-averaged electron densities. The Faraday interferometer measures the Faraday rotation angle of an electric field (due to the input laser signal) as well as the phase difference between input and output signals to measure the chord-averaged density and chord-averaged magnetic field.

5. Electron temperature measurements. This is done with localized electron cyclotron and Thompson scattering measurements.

6. Z_{eff} measurements by visible bremsstrahlung. Z_{eff} is a useful characteristic of the impurity level in the plasma and its ability to achieve ignition.

7. Ion temperature measurements through neutron spectroscopy.

8. A summary of the above diagnostics, the reconstruction of the plasma equilibrium from the above, and a discussion of other diagnostics (such as Langmuir probe diagnostics to measure the plasma edge electron temperatures and edge particle fluxes) used in tokamak plasmas.

2 Magnetic Diagnostics

At its most basic, the following consequence of Maxwell's equations, applied to a closed loop with N coils:

$$\oint \mathbf{E} \cdot d\boldsymbol{\ell} = -N \frac{\partial}{\partial t} \int_S \mathbf{B} \cdot d\mathbf{S}$$

Where $\oint$ is a loop integral taken around the closed path and S is the surface enclosed by the path. Thus, the typical result being that the voltage drop across a closed surface:

$$V = -N \frac{d\Phi}{dt} \tag{2.1}$$

Where V is the voltage and Φ is the enclosed magnetic flux through the surface. To measure the local magnetic flux, the voltage is electronically integrated. Signal voltage integration then determines the magnetic flux through the coil. Furthermore, since magnetic fields within a tokamak possess an axis of symmetry (typically the fields may be modelled as axisymmetric), this allows for the determination of quasi steady-state current and magnetic field profiles along a surface by changing the orientation of the magnetic field. Furthermore, magnetic measurements through which a voltage is integrated can only be

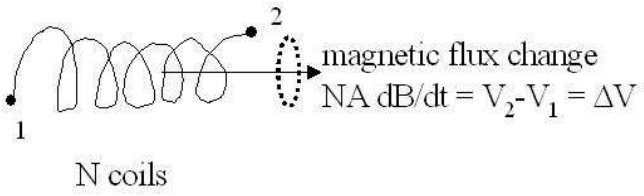

Figure 2.1: Diagram of a magnetic probe without associated integrated electronics. Varying magnetic flux through the solenoid of cross-sectional area A and with N loops induces a voltage drop between the ends.

measured for frequencies $\tau_{\text{int}}^{-1} < \omega < (\mu_0 \sigma L w)^{-1}$, where L is the vacuum inductance of the inner wall, w is the width of the wall, σ the conductivity, and τ_{int} is the time constant of the integrator.

2.1 Rogowski Coil, Voltage Loops, and Power Input to Tokamak

In order to characterize the total toroidal current in a tokamak, a Rogowski coil is used. A typical schematic, with associated signal integrating electronics is shown below:

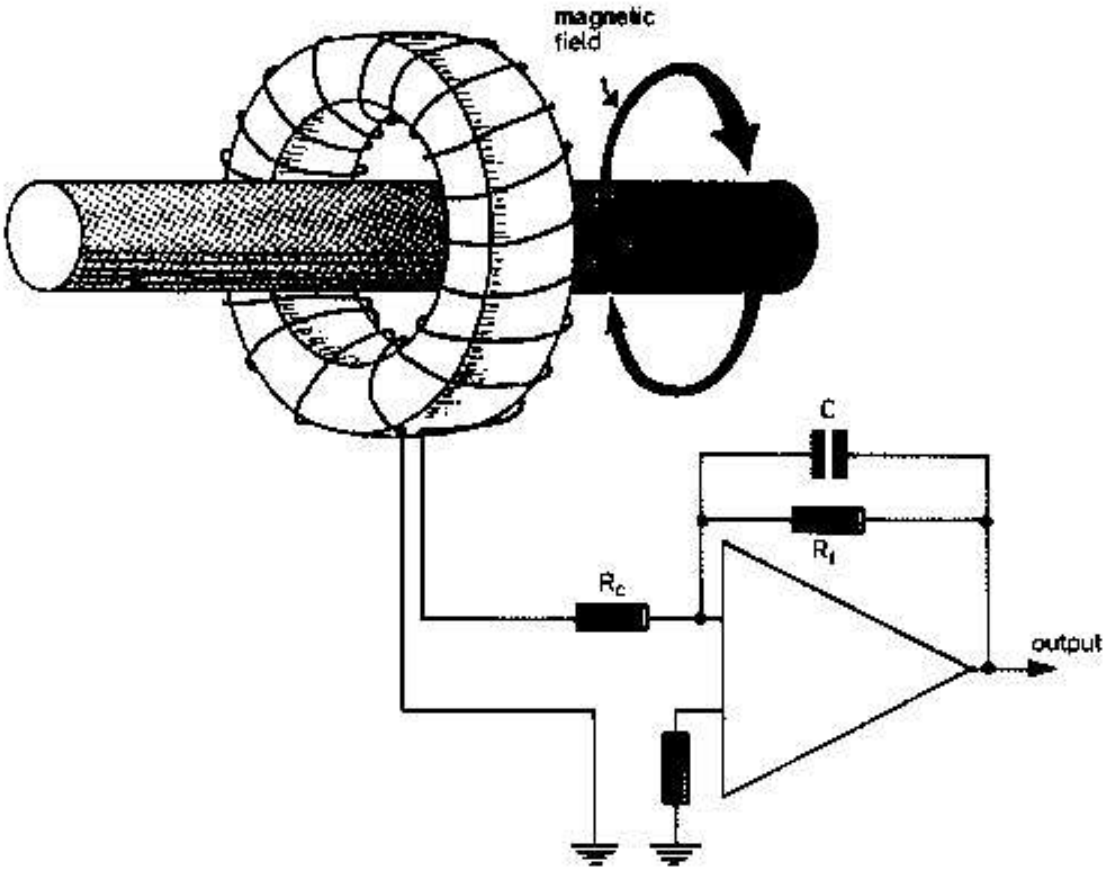

Figure 2.2: Diagram of a Rogowski coil, which measures total toroidal current in a tokamak. Also shown is the diode-based electronic integrator for the diagnostic.

As long as the variation in poloidal magnetic field between loops of the coil is small, such that $|\nabla B|/B \ll n$, where n is the turns (loops) per unit length (or equivalently $1/n$ is the length of wire per loop).

Furthermore, the toroidal current:

$$\mu_0 I_\phi = \oint_L \mathbf{B} \cdot d\ell$$

The total magnetic flux through the coil:

$$\Phi = n \int_A \oint_L \mathbf{B} \cdot d\ell dA = nA\mu_0 I_\phi$$

So that the voltage drop through the coil:

$$V_{RG} = -\dot{\Phi} = -nA\mu_0 \dot{I}_\phi$$

Which can be integrated to give the poloidal current. Furthermore, a toroidal loop measures the voltage across the tokamak, due to toroidal current-drive from a transformer. From these, the important estimates of a plasma in which the current is steady-state gives the following result:

$$P_{\text{plasma}} \approx I_\phi V_\phi \tag{2.2}$$

$$R_{\text{plasma}} \approx V_\phi / I_\phi \tag{2.3}$$

Where P_{plasma} is the power driven into the plasma, and R_{plasma} is the plasma resistance.

2.2 Poloidal and Toroidal Field Measurements

The magnetic field in an axisymmetric tokamak is given by the following, where Ψ is the poloidal flux and R is the radial distance from the axis of symmetry.

$$\mathbf{B} = \frac{1}{2\pi R}\mathbf{e}_\phi \times \nabla\Psi + B_\phi \mathbf{e}_\phi \tag{2.4}$$

With the following geometry of poloidal magnetic coils (to measure magnetic fields parallel to the surface) and toroidal voltage loops (to measure poloidal magnetic flux). The structure of the poloidal flux Ψ is determined partially by determining the boundary conditions on a closed surface S – the flux Ψ and the normal derivative at the surface, $\hat{\mathbf{n}} \cdot \nabla\Psi$, at specially chosen points.

The toroidal flux loop has voltage drop given by the following:

$$\begin{aligned} \oint \mathbf{E}_{\text{loop}} \cdot d\ell &= V_{\text{loop}} = -\int \mathbf{B}_p \cdot d\mathbf{A} \\ &= -2\pi \int_0^R \frac{r}{r}\frac{\partial \dot{\Psi}}{\partial r}\, dr = -\dot{\Psi}(R,z) \end{aligned}$$

The measurement of the derivative of magnetic flux normal to the surface at a given location is equivalent to measuring the poloidal flux normal at the surface. $\hat{\mathbf{n}}_0$ is the direction of the magnetic probe's flux surface, A is the area of the flux probe, N is the number of loops in the probe, and the voltage drop at the probe:

$$V_{\text{probe}} = -NA\dot{\mathbf{B}}_p \cdot \hat{\mathbf{n}}_0$$

In terms of the flux:

$$\mathbf{B}_p \cdot \hat{\mathbf{n}}_0 = \frac{1}{2\pi R}\hat{\mathbf{n}}_0 \cdot (\mathbf{e}_\phi \times \nabla\Psi) = \frac{1}{2\pi R}\nabla\Psi \cdot (\hat{\mathbf{n}}_0 \times \mathbf{e}_\phi) = \frac{1}{2\pi R}\hat{\mathbf{n}} \cdot \nabla\Psi$$

Where we have chosen an appropriate $\hat{\mathbf{n}}_0$ such that $\hat{\mathbf{n}}_0 \times \mathbf{e}_\phi = \hat{\mathbf{n}}$. Thus the measured probe voltage is proportional to $\hat{\mathbf{n}} \cdot \nabla\dot{\Psi}$:

$$V_{\text{probe}} = -\frac{NA}{2\pi R}\hat{\mathbf{n}} \cdot \nabla\dot{\Psi} \tag{2.5}$$

With information on the current profile within the tokamak (which is typically characterized by line-averaged Faraday rotation with an interferometer) and the boundary conditions, the profile of the equilibrium magnetic field may be derived. The loop voltage at any point is dominated by the large, relatively constant magnetic field induced by transformer; therefore differences in the loop voltage allows for a determination of the poloidal flux at the plasma edge.

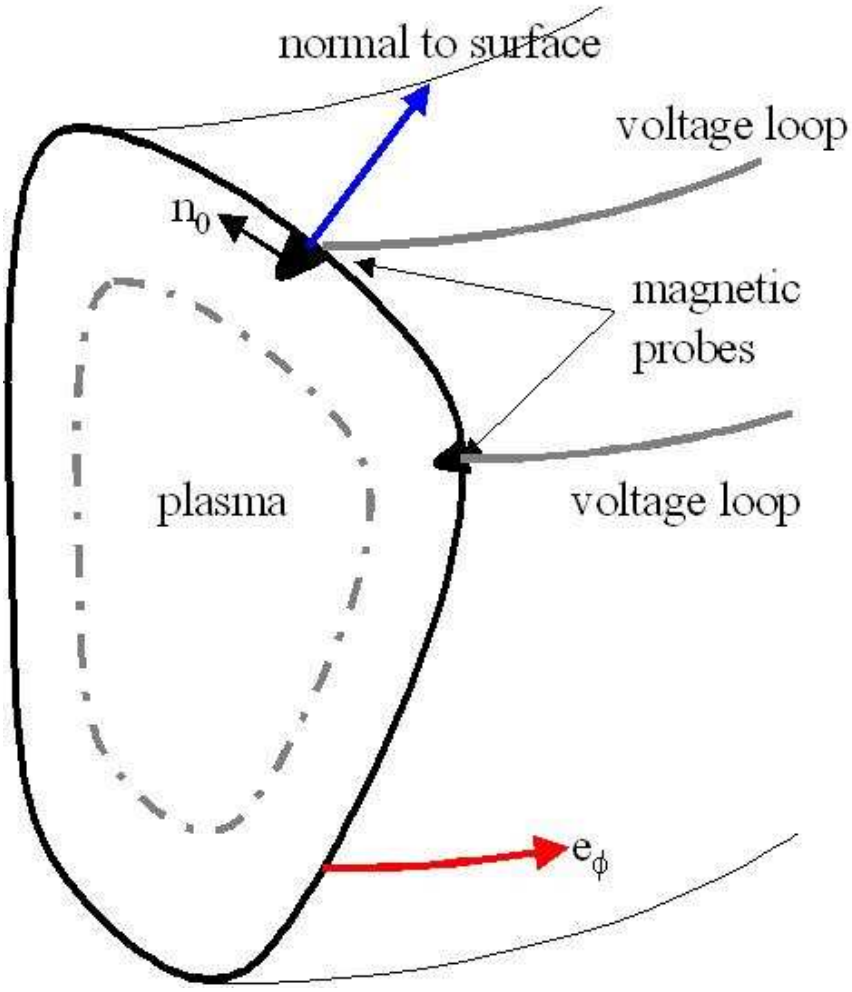

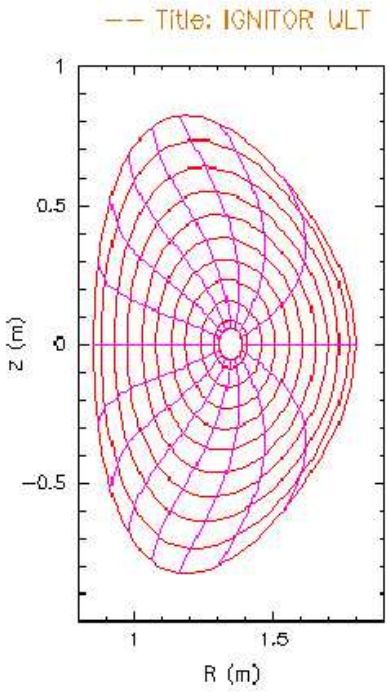

Figure 2.3: External measurements of the poloidal magnetic field, via the use of magnetic probes to measure $\hat{\mathbf{n}} \cdot \nabla \Psi$ and toroidal voltage loops to measure Ψ, at specific locations. Shown here is the orientation of the poloidal field coils $\hat{\mathbf{n}}_0$ relative to the surface normal $\hat{\mathbf{n}}$ and the toroidal unit vector $\mathbf{e}_\phi$. Furthermore, the diagnostic equipment is located in the vacuum between the inner surface (which encloses the plasma) and the outer surface.

Figure 2.4: On right is the *Boozer* coordinate profile of the proposed Ignitor toroidal fusion device. Magnetic probes are to be placed externally from the enclosed plasma along the outer edge at equal azimuthal Boozer coordinates. This diagram is taken from[7].

Similar, but displaced, probes are used in determining the external toroidal field – probes whose surface normal is aligned along $\mathbf{e}_\phi$.

2.3 Diamagnetic Measurements

An estimate of the kinetic energy, and hence plasma β, within the bulk plasma can be arrived at by examining the radial force balance equation, where although magnetic energy density is dominated by the toroidal field B_ϕ, the magnetic tension is dominated by the poloidal field:

$$\frac{\partial p}{\partial r} + \frac{\partial}{\partial r}\left(\frac{B_\phi^2}{2\mu_0}\right) + \frac{1}{r}\frac{\partial\left(rB_\theta\right)}{\partial r}\frac{B_\theta}{\mu_0} = 0 \tag{2.6}$$

Multiplying by r^2 and integrating by parts, we have the following result:

$$\begin{aligned} &-2\mu_0\int_0^a p(r)r\,dr - \int_0^a B_\phi^2 r\,dr + \frac{1}{2}B_\phi(a)^2a^2 + \frac{1}{2}a^2B_\theta(a)^2 = 0 \\ &\beta_\phi = \frac{2\mu_0\left\langle p\right\rangle}{B_{\theta a}^2} = 1 + \frac{B_{\phi a}^2 - \left\langle B_\phi^2\right\rangle}{B_{\theta a}^2} \end{aligned}$$

Where a is the minor axis of the tokamak.

$$\begin{aligned} &\left\langle B_\phi^2\right\rangle = \frac{\int_0^a B_\phi(r)^2\,r\,dr}{\int_0^a r\,dr} = \frac{2}{a^2}\int_0^a B_\phi(r)r\,dr \\ &\left\langle p\right\rangle = \frac{2}{a^2}\int_0^a p(r)r\,dr \\ &B_{\theta a} = B_\theta(r=a) \\ &B_{\phi a} = B_\phi(r=a) \end{aligned} \tag{2.7}$$

For tokamaks with small aspect ratio and low $\beta_\phi = 2\mu_0\left\langle p\right\rangle / B_{\phi a}^2 \ll 1$, one can show that $B_{\phi a}^2 - \left\langle B_\phi^2\right\rangle \approx 2B_{\phi a}\left(B_{\phi a} - \left\langle B_\phi\right\rangle\right)$.

In the limit of $\beta_\theta \sim 1$, β_θ is an appropriate measure of the plasma kinetic energy:

$$\beta_\theta = 1 + \frac{2B_{\phi a}\left(B_{\phi a} - \left\langle B_\phi\right\rangle\right)}{B_{\theta a}^2} \tag{2.8}$$

In the limit of large β_θ, when the toroidal current and hence poloidal field go to zero, the appropriate

measure of the plasma kinetic energy becomes:

$$\beta_\phi = \frac{2\mu_0 \langle p \rangle}{B_{\phi a}^2} = 2\frac{B_{\phi a} - \langle B_\phi \rangle}{B_{\phi a}} \tag{2.9}$$

Here $\langle B_\phi \rangle = \Phi_\phi / (\pi a^2)$ is measured by a *diamagnetic loop* wrapped around the minor axis.

In tokamaks, measurement of β_ϕ is measured due to the fact that $B_{\phi a}/B_{\theta a}$ (the ratio of toroidal to poloidal fields) is of the order of 10 or higher, and hence $\beta_\theta \gg 1$.

A very simple diamagnetic loop, which effectively measures the toroidal magnetic flux through the tokamak, is shown below:

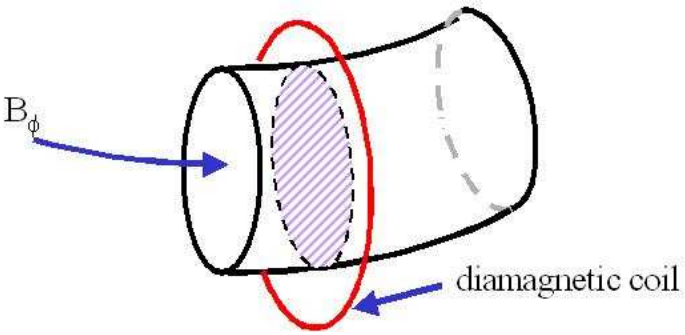

Figure 2.5: Simple diagram showing a diamagnetic loop. The input voltage is proportional to the time derivative of the total magnetic flux, so the input voltage is integrated to get a signal proportional to the flux $\pi r^2 \langle B_\phi \rangle$.

2.4 Other Magnetic Devices and Example Measurements

Other types of devices are the so-called saddle coils that measure the poloidal flux through the tokamak – unlike the toroidal voltage loops, these do not require the subtraction of flux due to the transformer. A diagram of the saddle coil is shown in Fig. (2.6) and measurements of global magnetic field quantities are shown in Fig. (2.7).

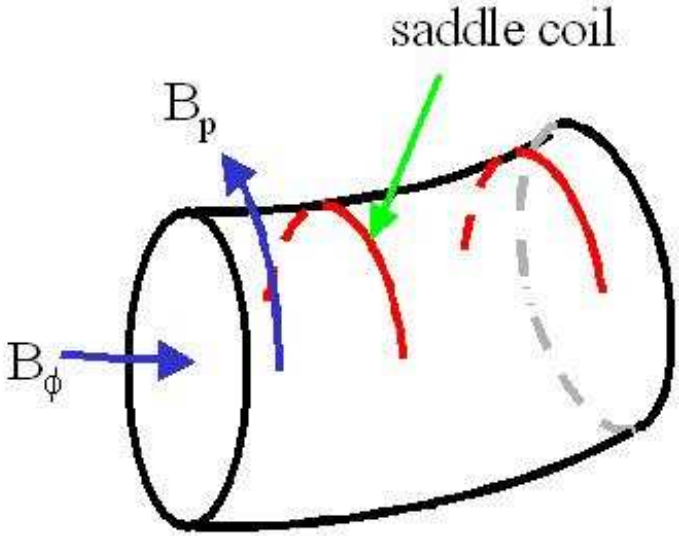

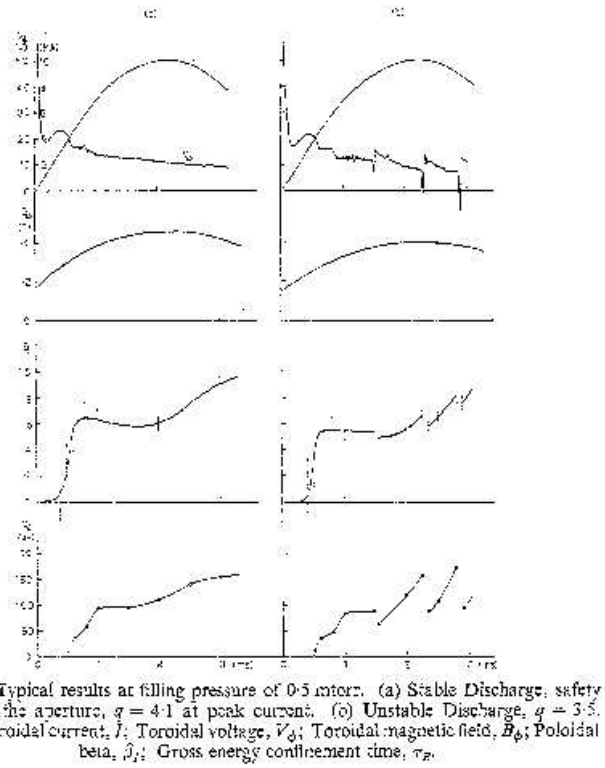

FIG. 2.—Typical results at filling pressure of 0·5 mtorr. (a) Stable Discharge, safety factor at the aperture, $q = 4{\cdot}1$ at peak current. (c) Unstable Discharge, $q = 3{\cdot}5$. Plasma toroidal current, I; Toroidal voltage, V_ϕ; Toroidal magnetic field, B_ϕ; Poloidal beta, β_p; Gross energy confinement time, τ_E.

Figure 2.6: On left is the saddle coil, measuring poloidal flux within a finite region of the tokamak, which does not require the subtraction of the transformer's inducing magnetic field.

Figure 2.7: On the right are some representative measurements of the tokamak voltage V_ϕ, toroidal current I_ϕ, poloidal magnetic beta, toroidal magnetic field at plasma edge, and the confinement time (defined as the plasma energy density/plasma power) in the Alcator C-Mod[8], and described in [2].

2.5 Introduction to Signal Integration and Differentiation

Suppose you have a signal and you wish to integrate or differentiate the signal. The following below show standard electronic devices to integrate and differentiate an input voltage signal from, for example, one of the magnetic devices shown above.

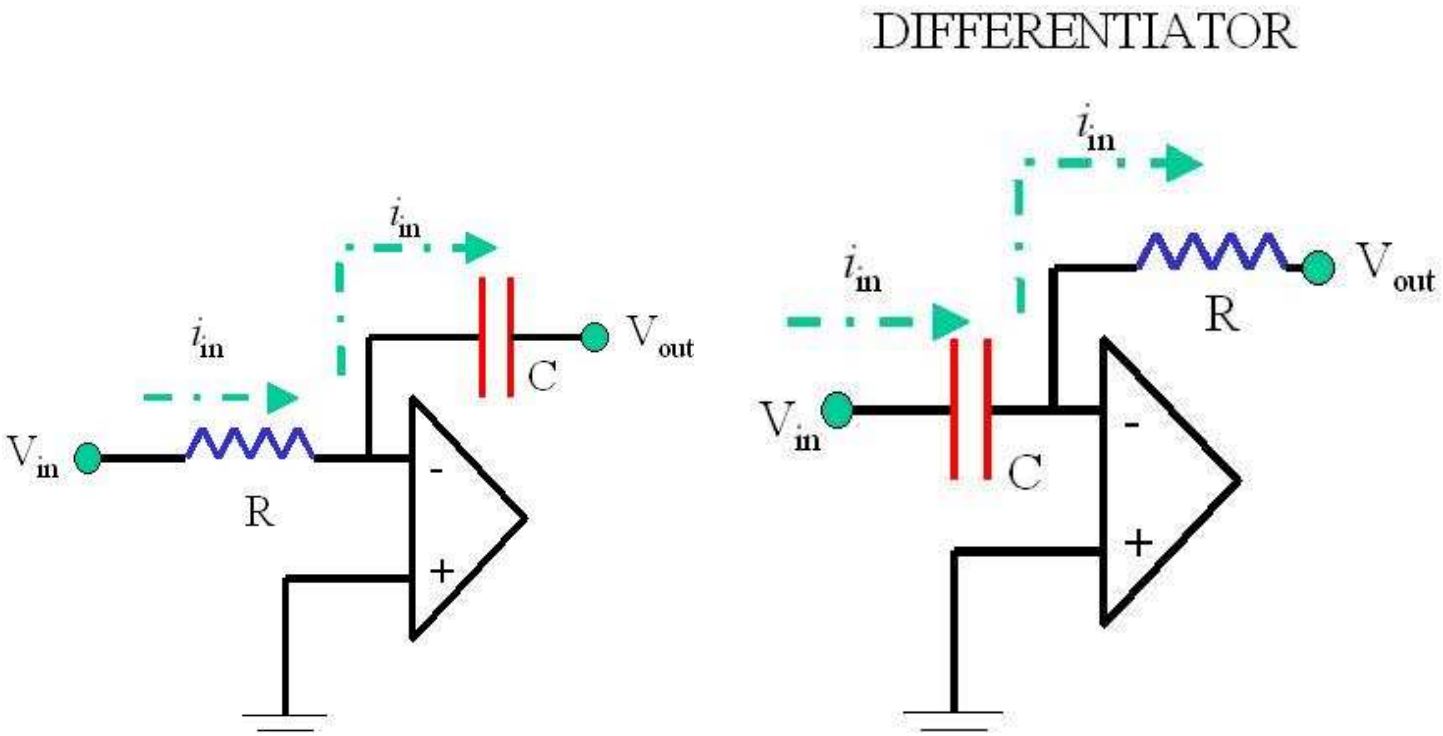

Figure 2.8: On left is electronic model of an integrator, and on left an electronic model of the differentiator, both with resistors of reistance R and capacitors of capacitance C (with time constant $\tau = RC$). Diodes are used to ensure a much better electronic bandpass for the input signal transformation.

For the integrator, one can show that the current flowing towards the negative terminal of the diode:

$$i_{\text{in}} = V_{\text{in}}/R$$

And the output voltage (the voltage through the capacitor):

$$V_{\text{out}} = \frac{q}{C} = \frac{1}{C}\int_{-\infty}^{t} i_{\text{in}}\, dt' = \frac{1}{RC}\int_{-\infty}^{t} V_{\text{in}}\left(t'\right)\, dt'$$

While the output voltage across the differentiator is given by:

$$i_{\text{in}} = \frac{dq_{\text{in}}}{dt} = C\frac{dV_{\text{in}}}{dt} = V_{\text{out}}/R$$
$$V_{\text{out}}(t) = RC\frac{dV_{\text{in}}}{dt}$$

3 The Radiation from Free Nonrelativistic Electrons

Three important measurements to characterize a plasma arise from radiation emitted by free electrons taken, in this approximation, to arise within a vacuum. These three types of measurements are the following:

- Thompson scattering measurements and electron cyclotron emission to characterize the electron temperature distribution at a specific location.
- Visible bremsstrahlung emission by electrons colliding on ions that allows for a determination of $Z_{\text{eff}}^2 = \sum_i n_i Z_{\text{eff}}^2 / n_e$, a determination of the impurity level within the plasma.

Here, we consider radiation arising from nonrelativistic electrons. This is a relatively good approximation for the electron temperatures (of order a few keV) within a toroidal fusion confinement plasma.

Consider the radiation field from charged particles. Here, we work in Lorentz gauge so that the electric potential Φ and magnetic potential $\mathbf{A}$ due to a single charged particle is given by:

$$\Phi = \int \frac{\rho\left(\mathbf{r}', t - \left|\mathbf{r}' - \mathbf{r}\right| / c\right)}{4\pi\epsilon_0 \left|\mathbf{r}' - \mathbf{r}\right|} d^3\mathbf{r}' = \frac{Ze}{4\pi\epsilon_0 \left(R\left(t'\right) - \boldsymbol{\beta}\left(t'\right) \cdot \mathbf{R}\left(t'\right)\right)} \tag{3.1}$$

$$\mathbf{A} = \int \frac{\rho\boldsymbol{\beta}\left(\mathbf{r}', t - \frac{|\mathbf{r}'-\mathbf{r}|}{c}\right)\left(\mathbf{r}', t - \frac{|\mathbf{r}'-\mathbf{r}|}{c}\right)}{4\pi\epsilon_0 c \left|\mathbf{r}' - \mathbf{r}\right|} d^3\mathbf{r}' = \frac{Ze\boldsymbol{\beta}\left(t'\right)}{4\pi\epsilon_0 c \left(R\left(t'\right) - \boldsymbol{\beta}\left(t'\right) \cdot \mathbf{R}\left(t'\right)\right)} \tag{3.2}$$

$$\mathbf{R}\left(t'\right) = \mathbf{r} - \mathbf{r}_p\left(t'\right) \tag{3.3}$$

$$t' = t - R\left(t'\right)/c \tag{3.4}$$

Where t' is the retarded time, and t is the observer time, and $\mathbf{r}_p\left(t'\right)$ is the position of the particle *observed* at observer time t. $\boldsymbol{\beta} = \mathbf{v}/c$ is the normal relativistic β.

The only portion of the electric and magnetic field that contributes to the outward radiation of energy from the accelerating particle is, in the nonrelativistic limit and seen by an observer very far from the

particle (thus $R \gg r_p$, where $\mathbf{r}_p$ is the particle trajectory).

$$\mathbf{E}_{\text{rad}} \approx \frac{Z^2 e^2}{8\pi^2 \epsilon_0 c^3 r} \left(\hat{\mathbf{R}}(t') \times \left(\hat{\mathbf{R}}(t') \times \mathbf{a}(t') \right) \right) \tag{3.5}$$

$$\mathbf{B}_{\text{rad}} = \hat{\mathbf{R}}(t') \times \mathbf{E}_{\text{rad}} \tag{3.6}$$

$$\hat{\mathbf{R}} = \mathbf{R}/R \approx \text{constant} \tag{3.7}$$

Here, we neglect all relativistic effects (terms of order β or higher).

Furthermore, the energy flux measured by an *observer* is given by:

$$\frac{dP_{\text{obs}}}{d\Omega} = \frac{1}{\mu_0 c} |E|^2 r^2 = \frac{Z^2 e^2}{8\pi^2 \epsilon_0 c^3} \left| \hat{\mathbf{R}}(t') \times \left[\hat{\mathbf{R}}(t') \times \mathbf{a}(t') \right] \right|^2 \tag{3.8}$$

Where $dP_{\text{emitted}}/d\Omega$ is the power radiated per unit solid angle by the charged particle in its own reference frame, which for nonrelativistic particles is equal to the observed power to lowest order in β.

4 Introduction to Abel Inversion

The following are plasma diagnostics that do not allow for direct measurements.

1. From interferometric measurements of the phase difference between a reference arm and a measurement arm one can determine the line-averaged plasma density $\int n_e(s)\,ds$
2. From measurements of the rotation angle of an electric field through an intervening magnetic field, one can measure the line-averaged quantity $\int n_e(s)\mathbf{B}\cdot d\mathbf{s}$.
3. One can likewise determine the profile of the electron density by sweeping through a range of microwave frequencies and determining the position of reflection as a function of frequency.
4. measurement of the bremsstrahlung continuum spectrum must be made across different chords to characterize the Z_{eff}, and hence ion impurity, spatial profile.
5. The ion temperature has a specific profile in space and time. The emissivity of neutrons are not highly localized in energy or in space.

By measuring across multiple chords or frequencies, and exploiting the spatial symmetries of the plasma, one can then determine the profiles of density (interferometry or reflectometry), poloidal magnetic fields (Faraday rotation), ion temperature (neutron spectrometry), and impurity level (visible bremsstrahlung continuum). All these measurements share a common feature, namely that they require for their measurement an Abel inversion of the averaged data.

To perform an Abel inversion, one must impose a specific symmetry on the system. For stellarators and tokamaks, quantities are taken to be symmetric about the minor axis. Thus, for integrals of the following type, which could correspond to a phase measurement from interferometry with $f(r)$ being a density function:

$$F(y) = \int_{-\sqrt{a^2-y^2}}^{\sqrt{a^2-y^2}} f(r)\,dx = 2\int_y^a f(r)\frac{r\,dr}{\sqrt{r^2-y^2}} \tag{4.1}$$

One can perform an Abel inversion to get the function $f(r)$:

$$f(r) = -\frac{1}{\pi}\int_r^a \frac{dF}{dy}\frac{dy}{\sqrt{y^2-r^2}} \tag{4.2}$$

Of course, the inversions become more complicated if one assumes an angular dependence of the above quantities, and one must choose chordal measurements that expose the angular dependence. The theory of Abel inversions, and optimal choice of chordal measurements, is described in far greater detail in [2].

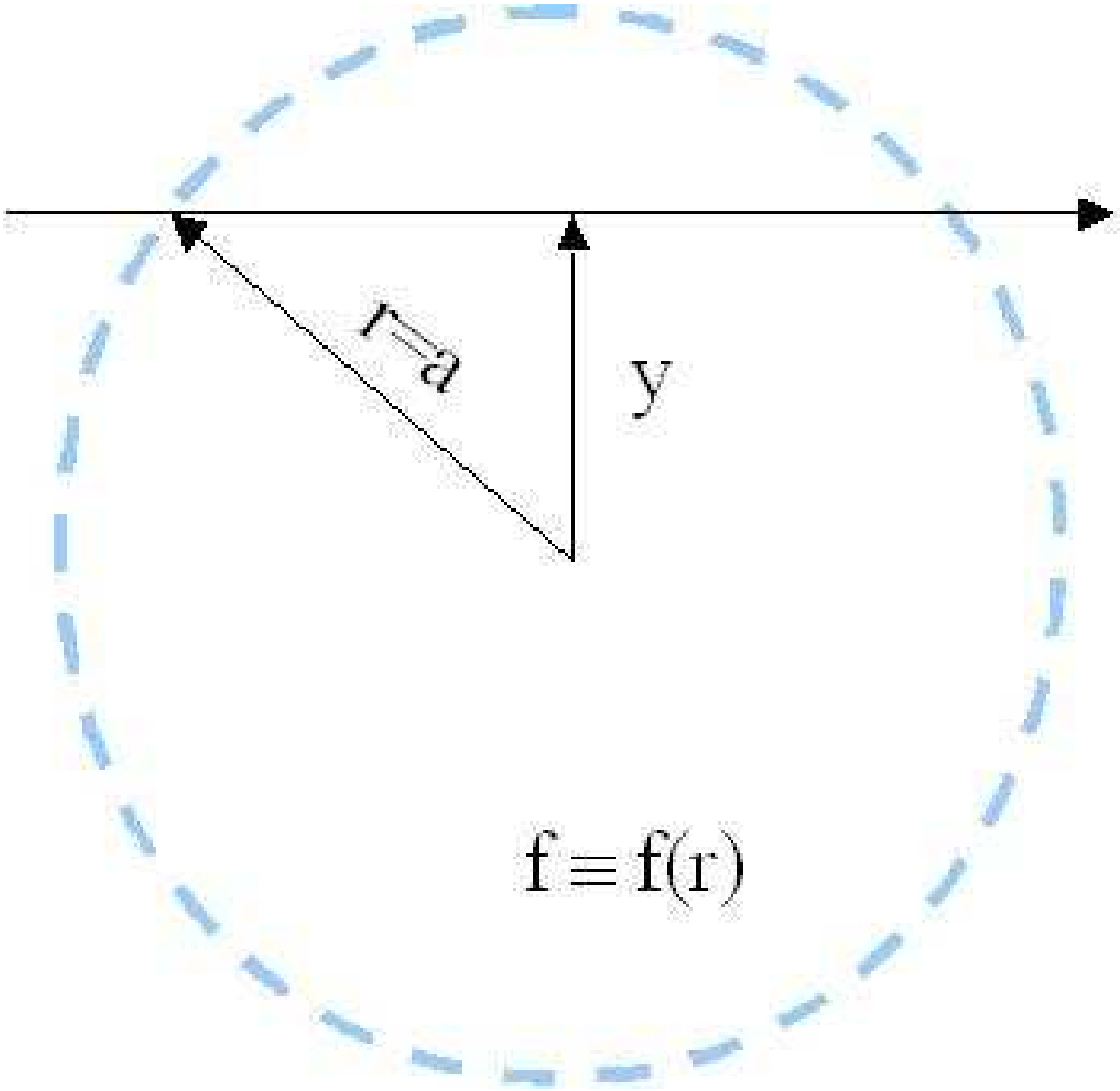

Figure 4.1: Essence of chordal measurements (say, total phase difference) of a variable (say, density) with radial symmetry, at different heights y in a plasma column of extent $r = a$.

5 Plasma Density and Internal Magnetic Field Measurements

5.1 Line-Averaged Plasma Density with Interferometry

The launch of an O-wave (electric field parallel to background magnetic field, propagation perpendicular to magnetic field) through intervening plasma results in a phase shift:

$$\Delta\phi = k\int^{L}\left(1-\sqrt{1-\frac{\omega_p^2}{\omega^2}}\right)ds \approx \frac{e^2}{2\epsilon_0 m_e \omega c}\int^{L} n_e(s)\,ds \tag{5.1}$$

relative to the same wave travelling through a vacuum (this is difference in phase from the reference arm relative to the measuring arm of the beam). Although the phase difference increases as ω^{-1}, however the angular deviation from refraction increases as ω^{-2}. The 10.6 μm emission from CO_2 lasers provides an accurate determination of phase with negligible refraction contributions to the phase.

A very basic Mach-Zender interferometer is shown in Fig. (5.1). The intensity $\propto |\mathbf{E}|^2$ of the interfered signal is measured. If we make the simplifying assumption that the reference and measurement arms must travel the same distance, then if the reference arm electric field is A, the measurement arm electric field is B, and the only phase acquired is through the plasma traversal:

$$\begin{aligned} I_{\text{in}} &= (A+B)^2 \\ I_{\text{out}} &= \left|Ae^{i\Delta\phi}+B\right|^2 = A^2+B^2+2AB\cos\Delta\phi \end{aligned} \tag{5.2}$$

Measurement of the phase difference allows one to determine the line-averaged plasma density.

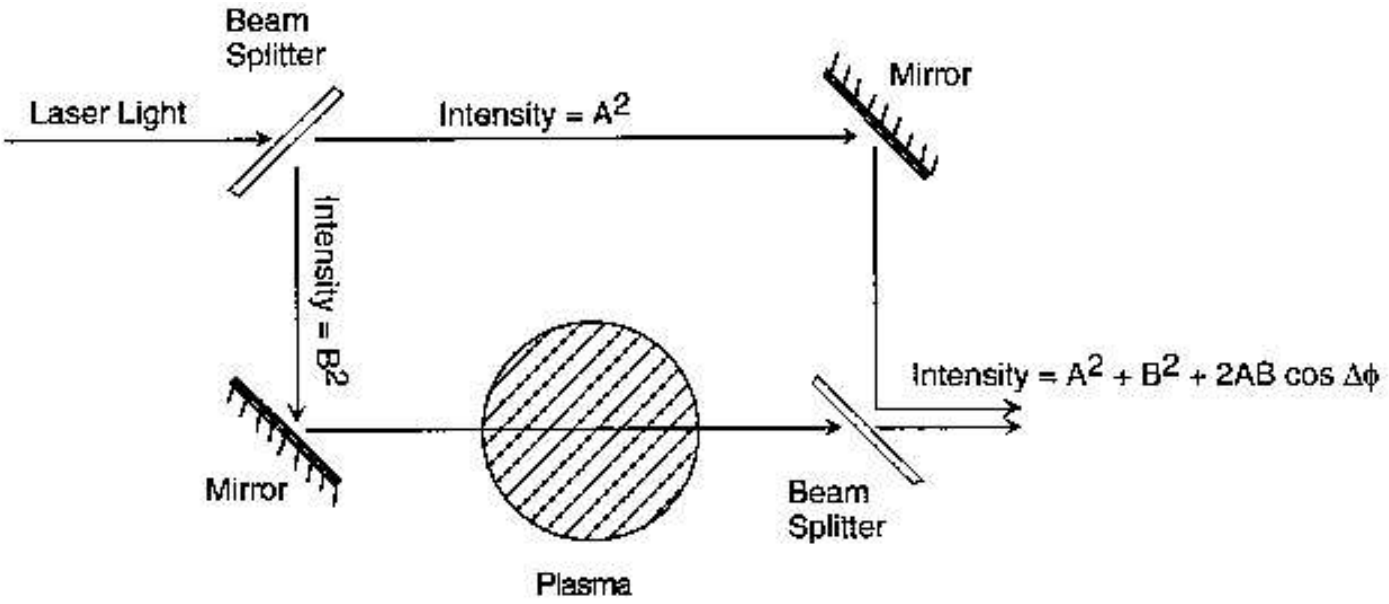

Figure 5.1: Mach-Zender interferometer to measure line-averaged plasma density. Interferometers in measure density through multiple chords through the plasma simultaneously.

This apparatus suffers from the fact that what is measured is the total phase, due to the plasma as well as due to the changing of arms from seismic or other effect. Systems that use an interferometric setup with one laser beam (such as CO_2) are generally quite large (few to ten meters across), their vibration isolation is correspondingly large and expensive, and it is therefore relatively easy for phase measurements, and hence density measurements, to be off by a few multiples of 2π.

A much better method is the two-color interferometer[9], in which a lower frequency laser such as CO_2 at 10.6 μm and a higher frequency HeNe laser at 6330 Å both traverse the plasma. The phase differences of the HeNe and the CO_2 laser due to seismic or other vibrations are correlated, so therefore the subtraction of one phase from the other gives a much less ambiguous measurement of plasma density.

In interferometric systems, vibrations on time scales much longer than the inverse frequency of the laser lights cause length changes in the interferometric apparatus of length $\tilde{L}$; a suitably designed interferometer will have the same change in length $\tilde{L}$ for both lasers. One can then express the change in phase for the

HeNe and CO_2 lasers as the following, with phase contributions due to the plasma and due to the vibration:

$$\bar{n}_e L\left(\frac{1}{2\pi} r_e \lambda_{CO_2}\right) + \frac{2\pi\tilde{L}}{\lambda_{CO_2}} = \Delta\phi_{CO_2}$$
$$\bar{n}_e L\left(\frac{1}{2\pi} r_e \lambda_{HeNe}\right) + \frac{2\pi\tilde{L}}{\lambda_{HeNe}} = \Delta\phi_{HeNe}$$
$$\bar{n}_e L = \int^L n_e(s)\, ds$$

Here r_e is the Thompson radius of the electron – defined by the fact that a shell of total charge e and radius r_e has potential energy equal to the electron rest energy:

$$r_e = \frac{e^2}{4\pi\epsilon_0 m_e c^2} \tag{5.3}$$

The chord-integrated density $\bar{n}_e L$ can be reduced to the following:

$$\bar{n}_e L = \frac{2\pi}{\lambda_{CO_2} r_e}\left(\frac{\Delta\phi_{CO_2} - \frac{\lambda_{HeNe}}{\lambda_{CO_2}}\Delta\phi_{HeNe}}{1 - \lambda_{HeNe}^2/\lambda_{CO_2}^2}\right) \tag{5.4}$$

A representative TCI setup with density measurements are shown in Fig. (5.2).

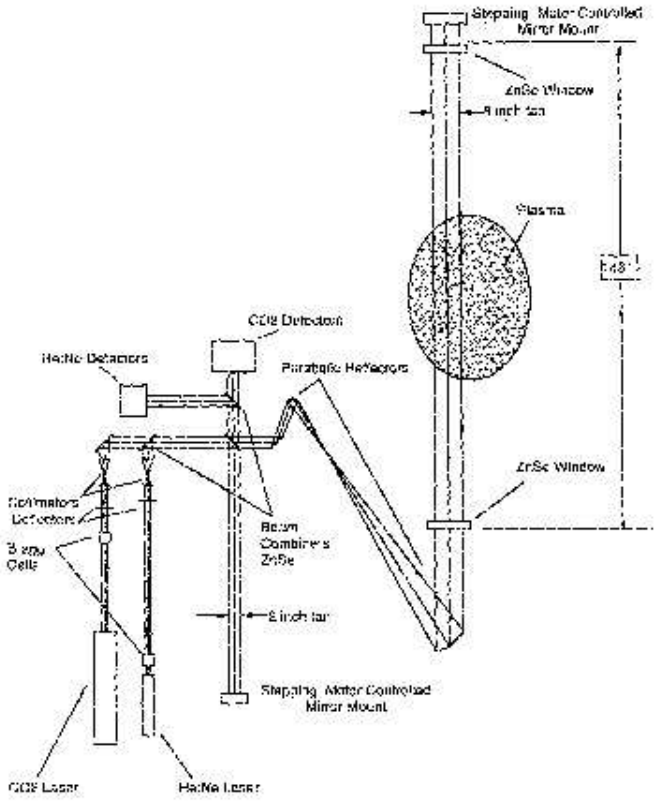

FIG. 1. General layout of the C-MOD two-color interferometer conceptual design system indicating major components. Note that the Bragg cells are oriented so that the first-order light is diffracted into the diagram. After collimation, two fan-shaped beams are produced at each wavelength, one above the other.

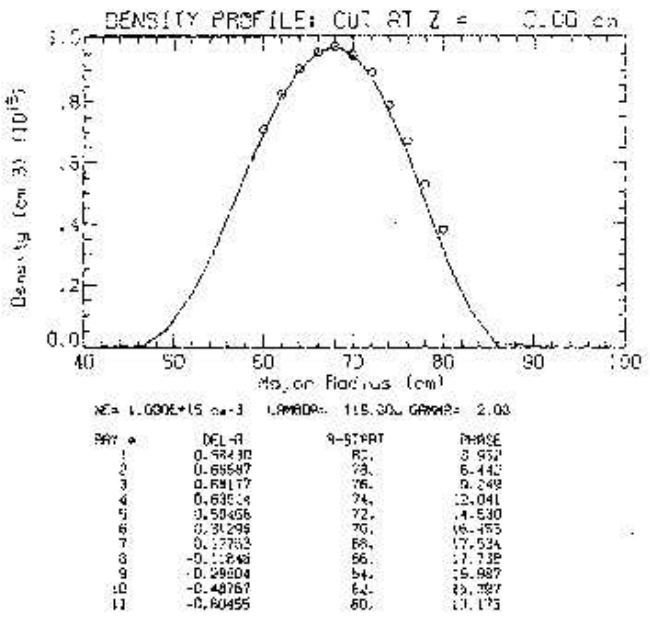

RAY #	DEL-R	R-START	PHASE
1	0.98430	82.	3.932
2	0.66587	78.	6.442
3	0.69177	76.	9.249
4	0.63514	74.	12.041
5	0.59456	72.	14.530
6	0.51296	70.	16.455
7	0.37763	68.	17.534
8	-0.11848	66.	17.738
9	-0.29504	64.	16.987
10	-0.48767	62.	15.397
11	-0.60455	60.	13.173

FIG. 2. Results from a ray tracing code are shown for a peak on-axis density of 1.0×10^{13} cm^{-3}. The solid line is the density profile of a radial cut at the midplane ($Z = 0$). The field-of-view through the C-MOD vertical ports covers the 60–80 cm range. The open circles are plots of the calculated $\langle n \ell \rangle$s from the code divided by the vertical distance between the upper and lower separatrix. R-START in the table indicates the chord radius on which the ray is started, DEL-R how far off the chord radius the ray moved in one pass, and PHASE is the single-pass phase shift along the chord. Note that the maximum deflection of the 119-μ beam is 0.68 cm.

Figure 5.2: Two-color interferometer setup, taken from [9].

5.2 Faraday Rotation and Polarimetry Measurements

In calculating the rotation angle due to a magnetic field, we take as before the WKB approximation with propagation nearly perpendicular to the magnetic field. X-modes launched in this manner will have their electric field polarization angle rotated by crossing a magnetic field.

The characteristic electric fields of the right-handed and left-handed waves, and their associated indices of refraction, are given by, in the limit of $\omega^2 \gg \omega_p^2$ and $\omega^2 \gg \Omega_{ce}^2$, where $\Omega_{ce} = -eB/m_e$ is the electron

cyclotron frequency:

$$\mathbf{E}_R \approx (1, i) \tag{5.5}$$
$$N_R \approx 1 - \frac{\omega_p^2}{2\omega^2}\left(1 - \frac{\Omega_{ce}}{\omega}\cos\theta\right) \tag{5.6}$$
$$\mathbf{E}_L \approx (1, -i) \tag{5.7}$$
$$N_L \approx 1 - \frac{\omega_p^2}{2\omega^2}\left(1 + \frac{\Omega_{ce}}{\omega}\cos\theta\right) \tag{5.8}$$

Where $\cos\theta$ is the angle between the direction of propagation and the magnetic field (assumed close to $\pi/2$). Consider an initial electric field is linearly polarized:

$$\mathbf{E}(0) = \frac{1}{2}E\,(1,0) = \frac{1}{2}E\,[(1,-i) + (1,i)]$$

The electric field after traversing a distance L:

$$\mathbf{E}(L) = E\exp\left(i\frac{\omega}{c}\int_0^L \frac{N_R + N_L}{2}\,ds\right)\left(\cos\left[\frac{\omega}{2c}\int_0^L (N_L - N_R)\,ds\right], \sin\left[\frac{\omega}{2c}\int_0^L (N_L - N_R)\,ds\right]\right) \tag{5.9}$$

Thus, in propagation within the magnetic plasma, one has information on both the line-averaged density (via interferometric measurements) and on the polarization angle. The phase change due to the plasma is given by Eq. (5.1), and the change in phase angle:

$$\alpha = \frac{\omega}{2c}\int_0^L (N_L - N_R)\,ds = \frac{\omega}{2c}\int_0^L \frac{\omega_p^2 eB/m_e}{\omega^3}\cos\theta\,ds = \frac{e}{2m_e c}\int_0^L \frac{n_e(s)\mathbf{B}(s)\cdot d\mathbf{s}}{n_c} \tag{5.10}$$

Where we have used the result $B\cos\theta\,ds = \mathbf{B}\cdot ds\mathbf{s}$ and the cutoff density n_c is defined as:

$$\omega^2 = \frac{e^2 n_c}{\epsilon_0 m_e} \tag{5.11}$$

An apparatus that measures the Faraday rotation is shown in Fig. (5.3) on the left, and Faraday rotation measurements as a function of distance from the major axis is shown on the right. These plots are taken from [10].

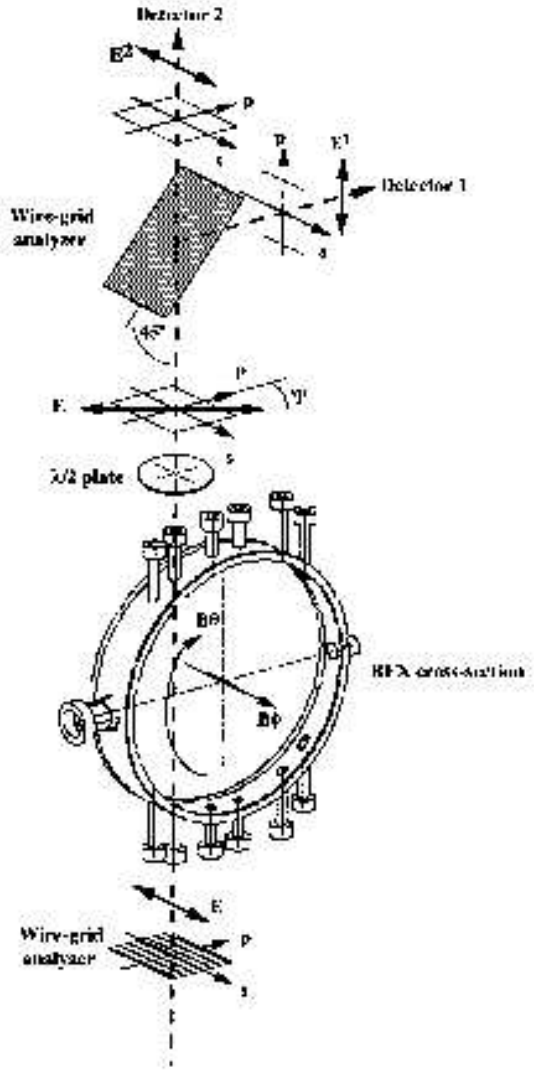

FIG. 1. Principle of operation.

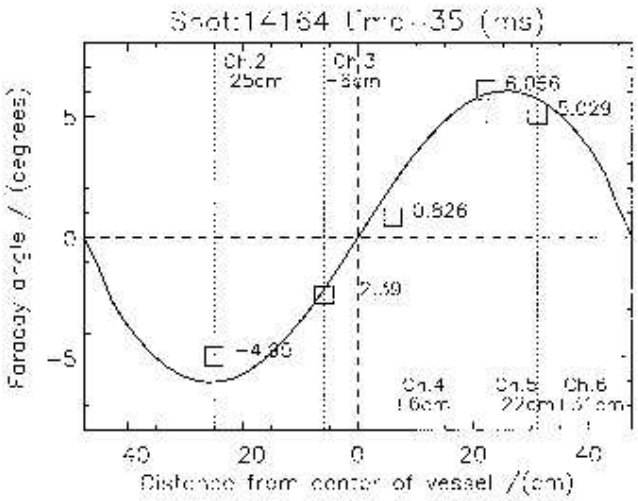

FIG. 4. Comparison of the measured and calculated Faraday angles at 35 ms.

Figure 5.3: On left is the schematic of an infrared laser Faraday polarimeter and interferometer. On right are measurements of Faraday rotation at different radii from the major axis.

5.3 Reflectometry Measurements

Equivalently, one may perform reflectometry measurements at frequencies of the order of the plasma frequency in the fusion device. Waves injected at frequency ω are reflected from the plasma where $\omega = \omega_p(x)$. The diagram shown below depicts this:

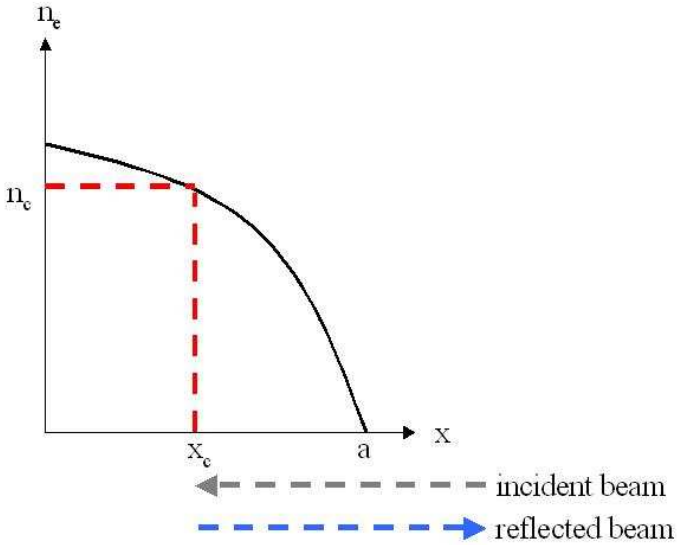

Figure 5.4: The principle of reflectometry. Plasma waves are reflected at x_c, where $n_c = n_e(x_c)$ and $e^2 n_c/(\epsilon_0 m_e) = \omega^2$. For the plasma densities $n_e \sim 10^{19}$ m^{-3}, the wavelengths of the waves used in reflectometry are $\lambda \sim 1$ cm, in the microwave. The plasma boundary is at $x = a$, where the density goes to zero.

Although time-of-flight measurements of the reflected wave can give an electron density profile, here we use the phase difference between the incoming and reflected wave. Assume an O-wave is launched by a microwave antenna into the plasma and neglect the effects of refraction. The differential equation that describes the form of the electric field E as a function of spatial position x:

$$\frac{d^2E}{dx^2} + \frac{1}{c^2}\left(\omega^2 - \omega_p(x)^2\right) E(x) = 0 \tag{5.12}$$

One can show from the WKB approximation with turning points [11, 12] that the phase difference between the incoming and reflected wave is at $x = a$, the plasma boundary:

$$\Delta\phi = \frac{2}{c}\int_a^{x_c} \left(\omega^2 - \omega_p^2\right)^{1/2} dx - \frac{\pi}{2} \tag{5.13}$$

Where x_c is the cutoff of plasma wave of frequency ω (see Eq. (5.11)). Through a frequency sweep, from very low frequencies to the maximum plasma frequency in the medium, a profile of the density $n_e(x)$ may be constructed. Furthermore, by an Abel inversion one can determine the cutoff position $x_c(\omega_c)$ as a function of the above phase difference measurements:

$$x_c(\omega_p) = x_0 + \frac{c}{\pi}\int_0^{\omega_p} \frac{d\phi/d\omega}{\sqrt{\omega_p^2 - \omega^2}}\, d\omega \tag{5.14}$$

Where x_0 takes into account the location of the plasma edge.

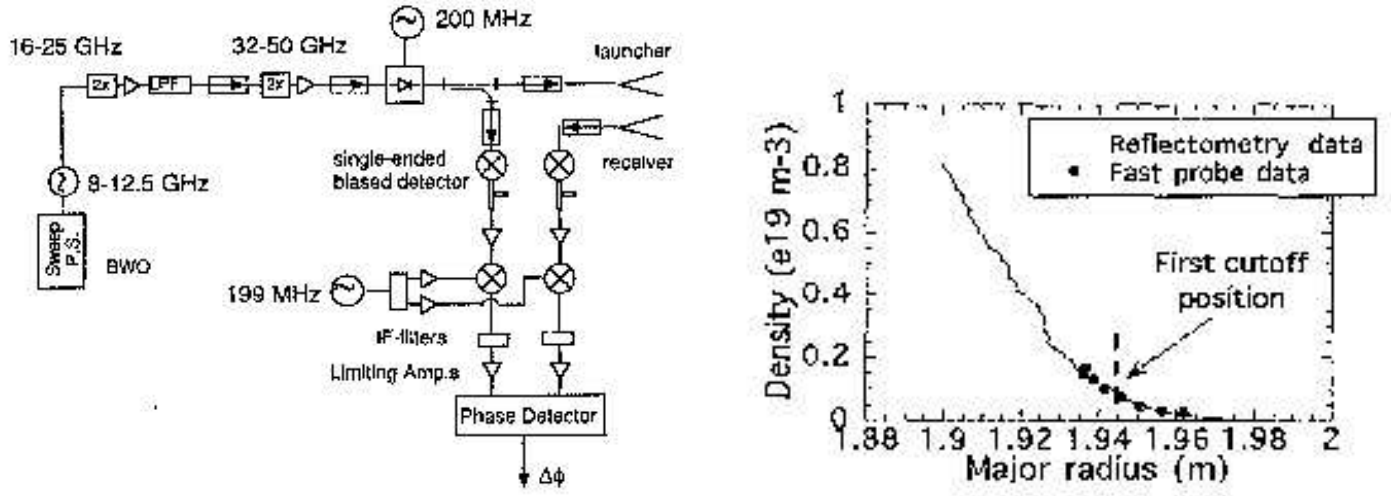

Figure 5.5: On left is schematic diagram of all relevant components in measuring phase differences through plasma reflectometry. On the right is a set of data taken from reflectometry, compared to Langmuir probe measurements, at the plasma edge. This data is taken from [13], measurements performed on a tokamak plasma.

6 Electron Temperature Measurements

6.1 Cyclotron Radiation and Electron Cyclotron Emission Measurements

6.1.1 Spectrum from Single Gyrating Particle

For a single charged particle undergoing gyromotion within a magnetic field, we define the speed parallel to the magnetic field $\beta_\parallel$ and speed perpendicular to be $\beta_\perp$. The radiation spectral power density per unit solid angle due to cyclotron emission seen at the observation point can be derived, including relativistic effects:

$$\frac{\partial^2 P_{\text{obs}}}{\partial\Omega_s \partial\omega} = \frac{Z^2 e^2 \omega^2}{8\pi^2 \epsilon_0 c} \sum_{m=1}^{\infty} \left(\left[\frac{\cos\theta - \beta_\parallel}{\sin\theta} \right]^2 J_m^2 \left(\frac{\omega}{\Omega_c} \beta_\perp \sin\theta \right) + \beta_\perp^2 {J'_m}^2 \left(\frac{\omega}{\Omega_c} \beta_\perp \sin\theta \right) \right) \times \frac{\delta\left(\left(1 - \beta_\parallel \cos\theta\right) \omega - m\Omega_c \right)}{1 - \beta_\parallel \cos\theta} \tag{6.1}$$

Where $\Omega_c = eB/m$ is the cyclotron frequency, θ is the angle between the observation point and the direction of the magnetic field. Resonances are observed at the frequencies

$$\omega_m = \frac{m\Omega_c}{1 - \beta_\parallel \cos\theta} \tag{6.2}$$

And J_m is the Bessel function of the first kind.

6.1.2 Plasma Emissivity Due to Cyclotron Emission

The plasma emissivity per unit volume, which is proportional the power emitted by the particles (rather than the power seen by an observer) is given by, for nonrelativistic plasmas, where f is the normalized distribution function.

$$j\left(\omega, \theta\right) = c^3 \int \frac{\partial^2 P}{\partial\omega \partial\Omega_s} \left(1 - \beta_\parallel \cos\theta\right) f\left(\beta_\perp, \beta_\parallel\right) 2\pi\beta_\perp \, d\beta_\perp \, d\beta_\parallel$$

For nonrelativistic plasma, in which $\beta \ll 1$, or in which $T \ll mc^2$, Doppler broadening of the cyclotron peaks ω_m results in the following profile of the plasma emissivity at frequencies in the vicinity of the

resonance peaks:

$$j(\omega,\theta) = j_m(\theta)\,\phi(\omega-\omega_m) \tag{6.3}$$

$$\phi(\omega-\omega_m) = \sqrt{\frac{m_e c^2}{2\pi T}}\frac{\exp\left(-\left(m_e c^2/2T\right)\left(\left[\omega-\omega_m\right]/\left[\omega_m\cos\theta\right]\right)^2\right)}{\omega_m\cos\theta} \tag{6.4}$$

$$\int \phi(\omega)\,d\omega = 1$$

$$j_m = \frac{Z^2 e^2 \omega_m^2 n}{8\pi^2\epsilon_0 c}\frac{m^{2m-1}}{(m-1)!}(\sin\theta)^{2(m-1)}\left(\cos^2\theta+1\right)\left(\frac{T}{2mc^2}\right)^m \tag{6.5}$$

In typical fusion plasmas, plasma emissivity due to cyclotron radiation is dominated by the lightest particles, the electrons. Furthermore, at typical temperatures of a few keV the electron distribution is largely nonrelativistic, and the emissivity profile about the cyclotron resonances allows for a determination of the local electron temperature through the width of the observed radiation profile.

6.1.3 Constraints on Plasma Intensity and Emissivity in Thermalized, Optically Thick Plasmas

The general expression for the measured intensity $I(\omega)$ of radiation at a given frequency (see, e.g. [14] for an introduction) is given by:

$$\frac{dI(\omega)}{ds} = j(\omega) - I\alpha(\omega) \tag{6.6}$$

Where ds is the differential unit of length along the light ray's path, and the optical depth τ that defines the absorption of the radiation along the ray path:

$$\tau = \int^s \alpha(\omega)\,ds \tag{6.7}$$

Furthermore, in an optically thick plasma the plasma intensity $I(\omega) = j(\omega)/\alpha(\omega)$. In typical tokamak plasmas the plasma intensity is thermalized, so that for frequencies of emission much less than the thermal energy, $\hbar\omega \ll T$, the blackbody intensity is given by the Rayleigh-Jeans approximation for low frequencies:

$$B(\omega) = \frac{\omega^2 T}{8\pi^3 c^2} \tag{6.8}$$

This is a good approximation of the energy spectrum in tokamaks, where the temperatures (in keV) are much larger than the energy $\hbar\omega$ of typical cyclotron emission.

In a tokamak device the spatial variation of the magnetic field results in a more extreme level of broadening than from Doppler effects. If we also assume that the wavelength of the radiation is much smaller than the length scale of magnetic field variations, then the WKB approximation implies that cyclotron resonant absorption and emission at frequency ω_0 is appreciable only when:

$$|m\Omega_e(s) - \omega_0| \ll \omega_0$$

Where $\Omega(s)$ is the cyclotron frequency at location s.

To lowest order the gradient of the magnetic field is constant along the light ray's path, so that $d\Omega_e/ds$ has a constant value. The optical thickness of radiation at frequency ω_0 can then be written as the following:

$$\tau_m = \int \alpha_m(\omega_0)\, ds = \alpha_m(s) \int \left|\frac{d\Omega_e}{ds}\right|^{-1} \phi(\omega_0 - m\Omega_e)\, d\Omega_e = \alpha_m(s) \left|\frac{d\Omega}{ds}\right|^{-1} \int \phi(\omega_0 - m\Omega_e)\, d\Omega_e$$

Since the line structure ϕ is very narrow, therefore the optical thickness about this frequency $\omega_0 = m\Omega(s)$ is given by:

$$\tau_m = \alpha_m(s) \left|\frac{d\Omega}{ds}\right|^{-1} \frac{1}{m} = \frac{L\alpha_m(s)}{m\Omega} \tag{6.9}$$

Where $L \equiv \Omega_e^{-1} \left|\frac{d\Omega_e}{ds}\right|^{-1}$ is the length scale of variation of the cyclotron frequency, and hence the magnetic field. Typically, for the lowest cyclotron resonances the $\alpha_m L \ll 1$ and the intensity at a given frequency ω_0:

$$I(\omega_0) = \frac{\omega_0^2 T(s)}{8\pi^3 c^2} \left(1 - e^{-\tau_m}\right) \approx \frac{\omega_0^2 T(s)}{8\pi^3 c^2} \tag{6.10}$$

From magnetic diagnostics the geometry of the magnetic field in a tokamak can be determined; one can then use the spectral intensity from ECE to determine the electron temperature profile within the plasma.

6.1.4 Electron Cyclotron Emission Diagnostics in Tokamak

Typically, ECE (electron cyclotron emission) measurements are measured from the low-field side of the tokamak; cyclotron emission is quite sensitive to the presence of a high-energy nonthermal tail of electrons. However, when viewing from the low-field side, the cyclotron emission from high-energy electrons will be absorbed by an optically thick intermediate region of thermal electrons. Typical ECE frequencies, for fusion tokamaks with toroidal magnetic fields on the order of a few to tens of Teslas, are in the range 60 - 600 GHz.

Furthermore, issues arise from cutoffs that may occur in the plasma. Typically the first or second cyclotron harmonics are optically thick. However, one can only measure electron temperatures only in regions where the cyclotron radiation does not meet a cutoff (i.e., where the wave becomes evanescent).

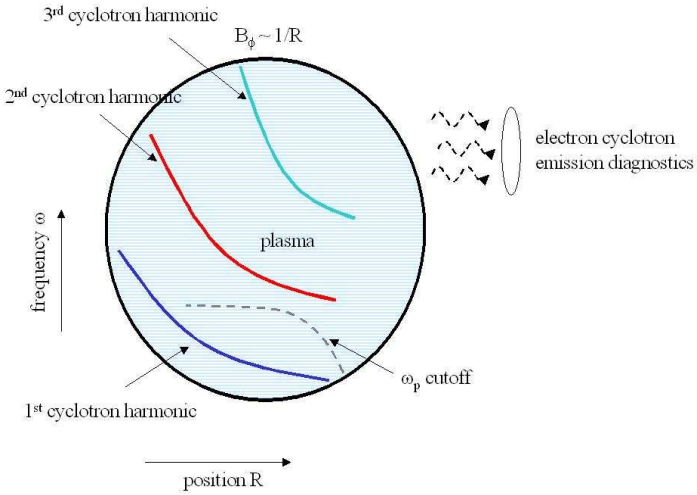

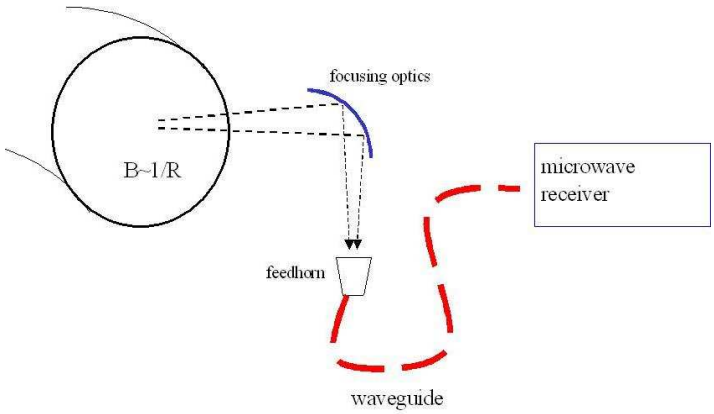

Figure 6.1: On left is a diagram depicting the plasma frequency cutoff and electron cyclotron harmonics in some represent tokamak. In general, one finds that, although the plasma is optically thick to first and second electron cyclotron harmonics, that one can measure a larger range of plasma densities, and hence more of the tokamak, when observing the X-mode second harmonic (X-mode propagation of frequency $\omega = 2\omega_{ce}$) than the O-mode first harmonic (which, as shown in this diagram, can only be accessed from a finite portion of the plasma). Other resonances (such as hybrid resonances) are not shown here. ECE measurements are taken from the low-field side.

Figure 6.2: On right is a mock-up of generic ECE measurements. Mirrors focus the radiation into a waveguide horn, through a transmission line, and into a remote receiver.

A polychromator is typically used to measure the temperature profile, with a time response of 5-10 μs and

a very good accuracy of the temperature profile relative to some carefully calibrated radiation source. A fixed temperature blackbody source is used for calibration of the instrumentation. A representative ECE instrumentation and observed electron temperature profile is shown below, for the TEXT-U tokamak at the University of Texas, Austin, for a relatively low temperature confined plasma:

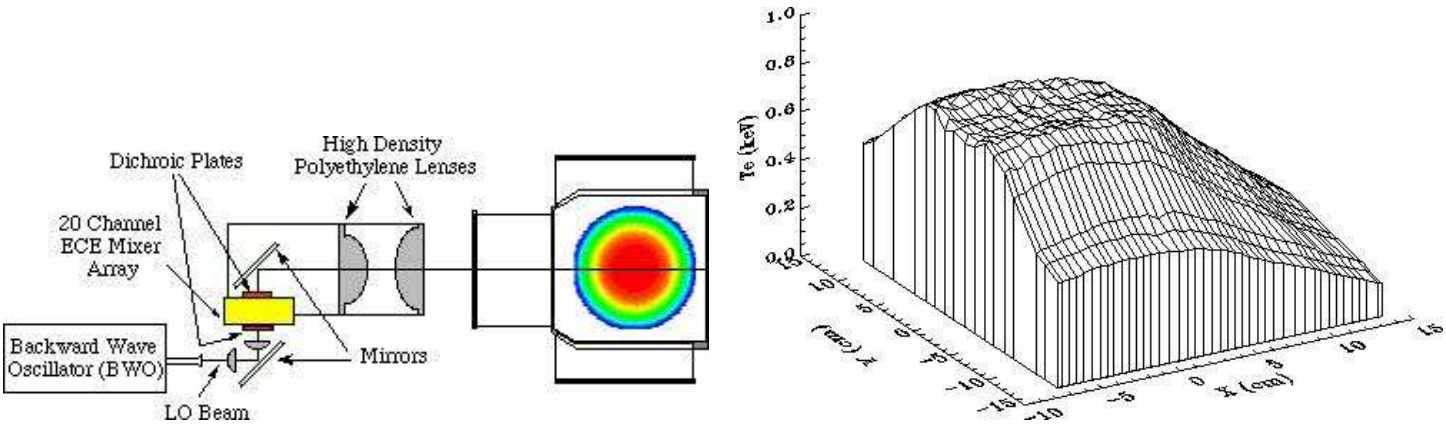

Figure 6.3: On left is microwave instrumentation for ECE measurements in the TEXT-U tokamak, and on right is electron temperature profile in a quiescent time shot (no sawteeth, tearing, or other instabilities that heat plasma locally), depicting smooth profile. Both these plots are taken from the `http://tempest.das.ucdavis.edu/ECE_New`.

6.2 Thompson scattering Measurements

6.2.1 Theory

Thompson scattering measurements are useful to diagnose the electron temperature in a specific location, rather than from a line average. For a typical fusion plasma, the small optical opening angles to properly resolve Thompson-scattered photons from a given location (large number of Thompson scattered photons), and the requirement that the background visible bremsstrahlung photons be small relative to the signal (short times), requires the use of short, intense laser pulses.

The bulk electron population is largely nonrelativistic in fusion devices. Furthermore, typically visible light (such as ruby lasers at 6943 Å) or infrared lasers provide the source of coherent incident radiation, so that $k\lambda_{De} \gg 1$ (wavelength much smaller than the electron Debye length) so that the scattering is incoherent; therefore the plasma emissivity due to Thompson scattering within a volume of plasma is the sum of the emissivity due to each electron.

With the above simplifications, the electron acceleration is given by an electric field $\mathbf{E}_i$.

$$\mathbf{a} = -\frac{e\mathbf{E}_i}{m_e}$$
$$\mathbf{E}_i = \tilde{\mathbf{E}}_i \exp\left(i\mathbf{k}_i \cdot \mathbf{r} - i\omega_i t\right)$$

Here the various terms associated with Thompson scattering in the nonrelativistic limit are given by:

$\mathbf{R} \equiv$ observed position vector of particle

$\omega_i \equiv$ frequency of incident wave

$\omega_s \equiv$ frequency of scattered (observed) wave

$\mathbf{k}_i \equiv$ wavenumber of incident wave

$\mathbf{k}_s = \hat{\mathbf{R}}\omega_s/c \equiv$ wavenumber of scattered wave

$\omega = \omega_s - \omega_i \equiv$ Thompson scattered frequency

$\mathbf{k} = \mathbf{k}_s - \mathbf{k}_i \equiv$ scattered wavevector

Given the above acceleration, and the definition of the electric field due to an accelerated charge in the far-field limit

$$\mathbf{E}_s(t) = \frac{e^2}{4\pi\epsilon_0 m_e c^2 R}\hat{\mathbf{R}} \times \left(\hat{\mathbf{R}} \times \mathbf{E}_i(t_r)\right) = \frac{r_e}{R}\boldsymbol{\Pi} \cdot \mathbf{E}_i(t_r) \tag{6.11}$$

Where $\boldsymbol{\Pi} = \hat{\mathbf{R}}\hat{\mathbf{R}} - \mathbb{I}$ in the nonrelativistic case is the tensor that extracts the component of $\mathbf{E}_i$ perpendicular to $\hat{\mathbf{R}}$, where r_e is given by Eq. (5.3). One can then show that the power per unit frequency per unit solid angle measured by an external observer is given by, where $\mathbf{e}$ is the normal vector in the direction of the electric field:

$$\frac{\partial^2 P}{\partial\omega_s \partial\Omega_s} = r_e^2 \left|\boldsymbol{\Pi} \cdot \mathbf{e}\right|^2 \langle S_i \rangle \, \delta\left(\mathbf{k} \cdot \mathbf{v} - \omega\right)\left(1 - \hat{\mathbf{R}} \cdot \boldsymbol{\beta}\right) \tag{6.12}$$

Where it has been assumed that over the area of incident beam, the electric field's vector orientation is unchanged (relevant for small solid angles subtended by the beam), and $\langle S_i \rangle = P_i/A$ refers to the incident

energy flux of the beam, where P_i is the beam power and A is the area subtended by the beam. In stating this result we assume that the particle's $\boldsymbol{\beta}$ remains constant.

The general plasma emissivity due to Thompson scattering in the nonrelativistic limit, where $v_k = \mathbf{k}\cdot\mathbf{v}/k = \omega/k$:

$$\begin{aligned} j\left(\omega_s, \Omega_s\right) &= \left(r_e^2 \int_V \left[S_i\right] \left|\hat{\mathbf{R}} \times \left(\hat{\mathbf{R}} \times \mathbf{e}\right)\right|^2 d^3\mathbf{r}\right) f_k \left(\frac{\omega_s - \omega_i}{\left|\omega_s \hat{\mathbf{R}}/c - \mathbf{k}_i\right|}\right) \left|\omega_s \hat{\mathbf{R}}/c - \mathbf{k}_i\right|^{-1} \\ f_k\left(v_k\right) &= \int f\left(v_k, \mathbf{v}_\perp\right) \, d\mathbf{v}_\perp \end{aligned} \tag{6.13}$$

The observed spectrum will track the electron distribution along the direction $\mathbf{k} = \omega_s \hat{\mathbf{R}}/c - \mathbf{k}_i$. This result holds for an uncorrelated magnetized plasma.

In the limit $\omega_i \gg \omega_p$ used in Thompson scattering measurements, the phase velocity ω/k in the distribution function f_k is given by:

$$v_k = \frac{\omega}{k} = c\frac{\omega_s - \omega_i}{\sqrt{\omega_s^2 + \omega_i^2}} \approx c\frac{\omega_s - \omega_i}{\omega_i\sqrt{2}}$$

The frequency width of the Thompson scattering spectrum:

$$\frac{\Delta\omega^2}{\omega_i^2} = \frac{2T_e}{m_e c^2} \ll 1 \tag{6.14}$$

6.2.2 Measurement

In Thompson scattering measurements, a laser beam provides a burst of photons, and optics subtending a small solid angle relative to the plasma at a specific location of the laser measure the Thompson-scattered photons. A very simplified schematic of a Thompson scattering apparatus is shown in Fig. (6.4).

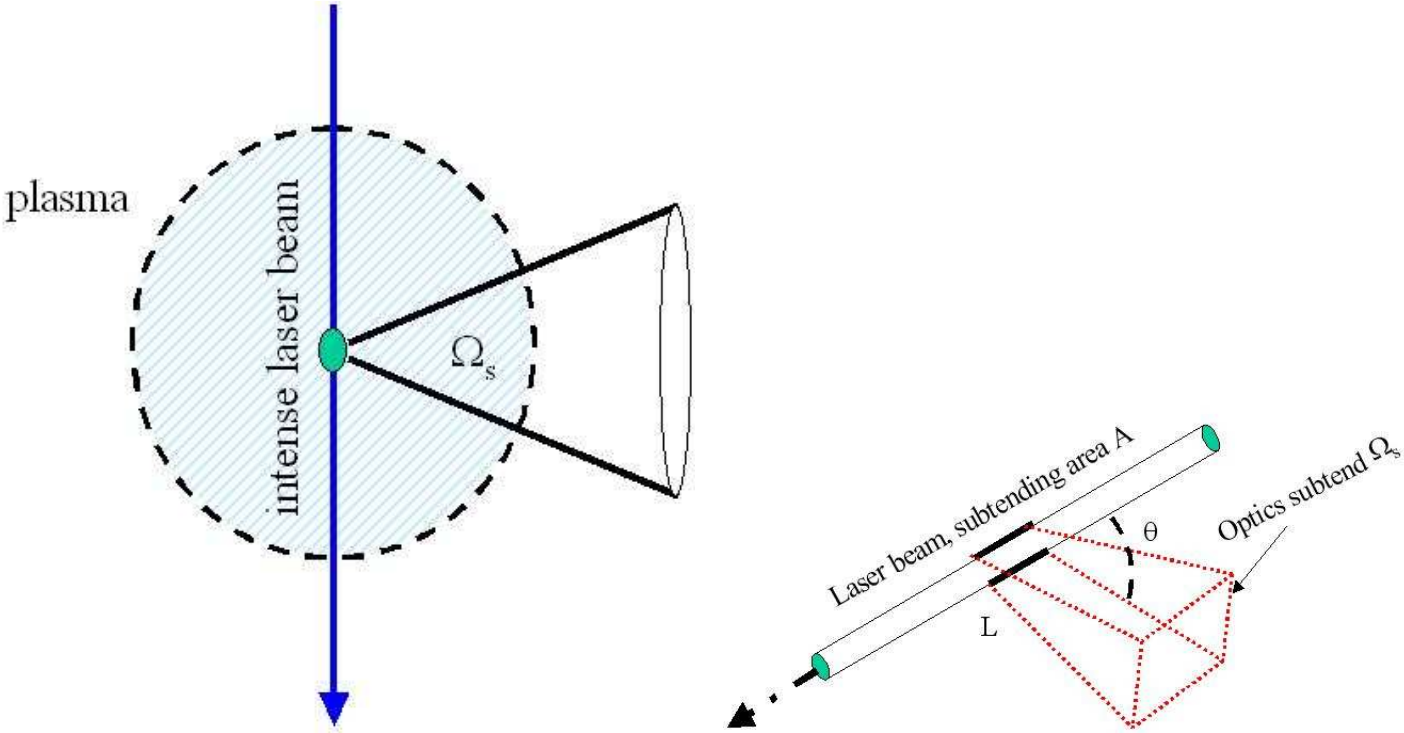

Figure 6.4: On the left is a very simplified cartoon depicting the a Thompson scattering measurement in a plasma. An intense laser beam with frequencies $\omega \gg \omega_p$ is sent through the plasma. Optics are typically positioned perpendicular to the propagation direction of the laser beam. The optics have a very small opening angle $\Omega_s \ll 1$ so that only Thompson-scattered photons at a specific location in the plasma along the laser (see green region in diagram) are collected from a region a few centimeters across.

On the right is a diagram depicting the geometry of collecting Thompson-scattered photons through optics located at an angle θ relative to the laser beam propagation. The beam has cross-sectional area A, and scattered photons are measured from a region L across the beam into an optical apparatus that subtends a solid angle Ω_s as seen from the measured region. Both diagrams are borrowed from [2].

Consider a system as shown in the above diagrams, with optics perpendicular to the electric field and the direction of propagation of incident radiation, so that $\left|\hat{\mathbf{R}} \times \left(\hat{\mathbf{R}} \times \mathbf{e}\right)\right| = 1$. The optics subtend a solid angle Ω_s and Thompson-scattered radiation from a length of plasma L along the beam is recorded. The total number of Thompson-scattered photons:

$$N_s = N_i r_e^2 \Omega_s n_e L$$

Where n_e is the local plasma density.

Note that for a typical plasma with electron temperatures $T_e \sim 1$ keV, the bandwidth of Thompson-scattered photons becomes $\Delta\omega/\omega_i \approx 30^{-1}$. For the 7000 Åincident ruby laser, this implies a wavelength bandwidth of 233 Å. Very special care must be taken that the signal is not masked by emission from impurities in the visible spectrum; this requires that the number of photons acquired from additional visible radiation sources in the scan time Δt must be much smaller than N_s, hence very high-power lasers, with energies of a few joules, operate over a short time periods (10-100 ns).

Finally, the efficiency of a given optical system to record photons is given by $Q < 1$, typically $Q \sim 10^{-2}$ for the given laser pulse. For typical plasma densities of (see figure) $n_e = 10^{13}$ cm^{-3}, with opening angles for the optics of 10^{-2} sr, with measurements localized about a region $L \sim 1$ cm, the observed number of photons:

$$QN_s = 2.8 \times 10^2 \text{ photons/joule}$$

The maximum signal-to-noise ratio, assuming that the source of photons is Thompson scattering, reduces to $S/N \rightarrow Q^{1/2}N_s^{1/2}$. However, this is generally not an accurate statement of the noise level in a Thompson scattering diagnostic, as reflections from the metal walls and line emissions can contribute on the order of the number of photons from Thompson scattering.

A typical Thompson scattering setup is shown in Fig. (6.5), taken from [15]. Note the relatively large contributions of stray laser light and plasma light in the diagnostic measurements of temperature and density.

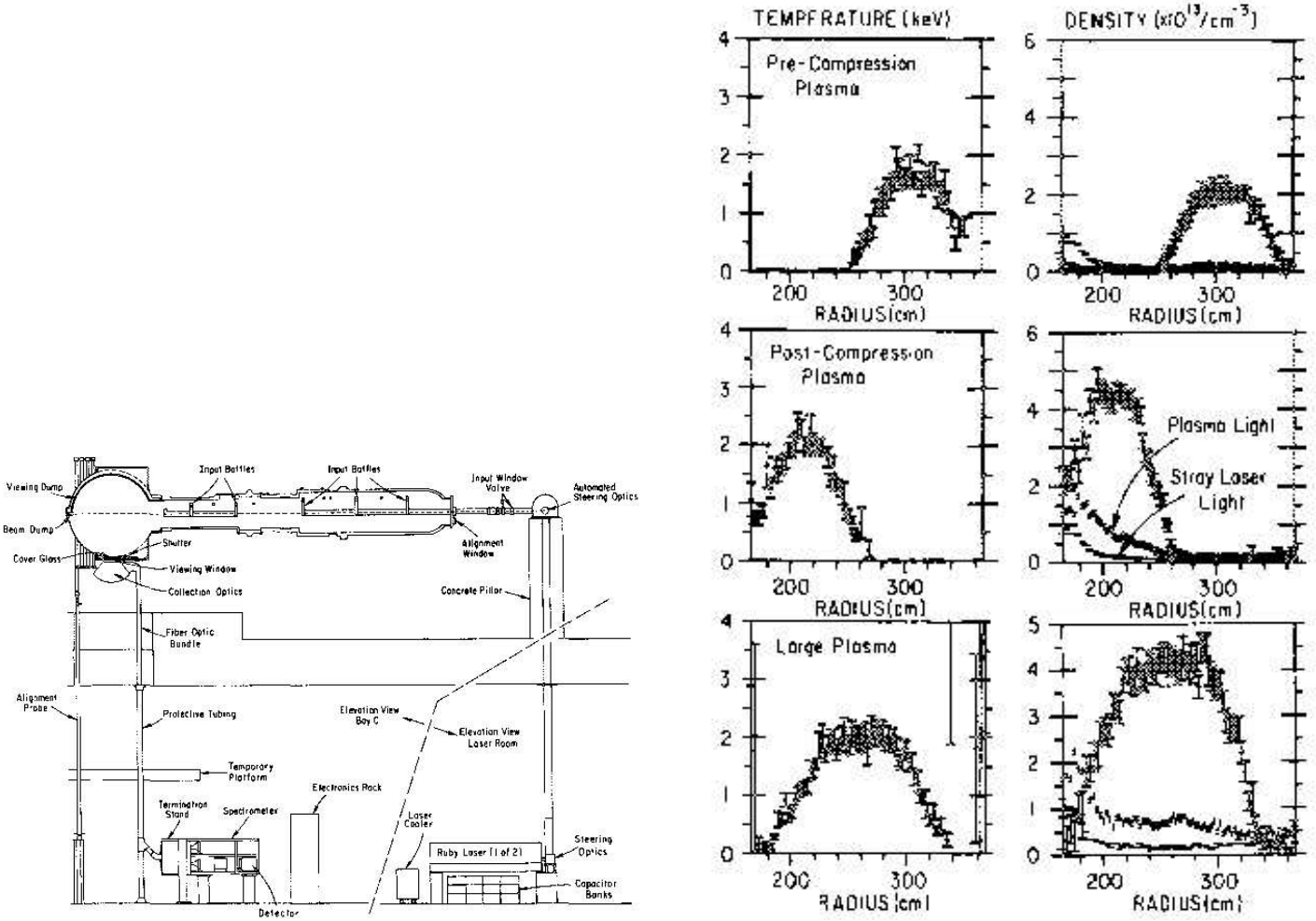

Figure 6.5: On left is the entire Thompson scattering setup, and on the right is the electron temperature and density profiles acquired from this setup, for various states of the plasma. Note the relatively significant levels of pollution arising from plasma light and stray laser light. Furthermore, in general it is much less difficult to measure plasma temperature than density; electron density measurements require a much more careful calibration of the instrumentation. Data are taken from [15].

7 Z_{eff} from Visible Bremsstrahlung Emission

7.1 Simplified Theory for Low-Energy Bremsstrahlung

Bremsstrahlung radiation in a plasma is dominated by electron-ion collisions. Electron-ion collisions can be modelled approximately as if ions are infinitely massive stationary force centers and electrons impact with incident velocity v_i.

In the approximation of an isotropic electron distribution, taken in the limit that one can ignore the effects of magnetic fields on particle orbits. Furthermore, since the electron distribution is isotropic as seen about the observation point, hence impacts can occur over all angles. Then the energy spectrum of radiation emitted by the electron due to the nonrelativistic collision is given by:

$$\frac{dW}{dt} = \frac{e^2}{6\pi^2\epsilon_0 c}\left|\int_{-\infty}^{\infty} \dot{\boldsymbol{\beta}} e^{i\omega t}\, dt\right|^2 \tag{7.1}$$

Where $\dot{\boldsymbol{\beta}}$ is the observed particle acceleration, localized in a region about the ion. One can calculate the acceleration of the particle using the energy equation for collisions and from the conservation of angular momentum, hence $r^2\dot{\theta} = v_1 b$, where v_1 is the incoming speed and b is the impact parameter.

$$\frac{1}{2}m\left(\dot{r}^2 + \frac{v_1^2 b^2}{r^2}\right) - \frac{Ze^2}{4\pi\epsilon_0 r} = \frac{1}{2}mv^2 \tag{7.2}$$

The radiation emitted from a single electron due to a density of n_i ion scatterers over all possible impact parameters b is then given by:

$$\frac{dP}{d\omega} = n_i v_1 \int_0^{\infty} 2\pi b \frac{dW}{d\omega}\, db = \frac{Z^2 e^6}{(4\pi\epsilon_0)^3}\frac{16\pi}{3\sqrt{3}}\frac{n_i}{m_e^2 c^3 v_1} G\left(\frac{i\omega b_{90}}{v_1}\right) \tag{7.3}$$

Where b_{90} refers to the impact parameter at incoming electron velocity v_1 that results in scattering by angle $\pi/2$, and G is the classical Gaunt factor, approaching 1 for $\omega \gg v_1/b_{90}$.

For an isotropic Maxwellian electron distribution with temperature T_e in a toroidal magnetic confinement plasma, for photon energies below the photoelectric edge of hydrogen atoms and hence of the thermal

energy of electrons ($\hbar\omega \ll 13.6$ eV $\ll T_e$):

$$\begin{aligned} j(\omega) &= n_e n_i Z_i^2 \left(\frac{e^2}{4\pi\epsilon_0}\right)^3 \frac{4}{3\sqrt{3} m_e^2 c^3} \left(\frac{2m_e}{\pi T_e}\right)^{1/2} \times \bar{g}_{ff} \exp\left(-\hbar\omega/T\right) \\ \bar{g}_{ff} &= \frac{\sqrt{3}}{\pi} \ln\left(\frac{4T_e}{\zeta\hbar\omega}\right) \end{aligned} \tag{7.4}$$

Where $\bar{g}_{ff}$ is the Gaunt factor for free-free interactions averaged over the distribution function, and $\zeta = e^{\gamma}$, where $\gamma \approx 0.5772$ is the Euler gamma constant. Typically, $\bar{g}_{ff}$ is taken to be 3 in measurements of the visible continuum and Z_{eff}.

From Eq. (7.4), the emissivity of visible bremsstrahlung allows for a determination of the Z_{eff}:

$$\begin{aligned} j(\omega) &\propto n_e^2 Z_{\text{eff}} \\ Z_{\text{eff}} &= \sum_j n_j Z_j^2 / n_e \end{aligned} \tag{7.5}$$

7.2 Z_{eff} Measurements Using Visible Bremsstrahlung

A properly calibrated visible continuum level can allow for the measurement of the Z_{eff} within the plasma is given by, for example, Schissel *et. al.*[16] that describes the Z_{eff} profile in the DIII-D tokamak. Using their calibrations, a local brightness (photons cm^{-3} Å sec):

$$\frac{dN}{d\lambda} = \frac{9.5 \times 10^{-14}}{\lambda} \bar{g}_{ff} n_e^2 T_e^{-1/2} Z_{\text{eff}} \exp\left(-hc/\left(\lambda T_e\right)\right)$$

Where n_e is electron density per cubic centimeter, T_e is electron temperature in eV, λ is light wavelength in Ångstroms, and $\bar{g}_{ff} = 3$ in these calculations. Here visible bremsstrahlung measurements are taken about 5230 Å with a 30 Å FWHM bandpass. Care must be taken to choose a bandpass for measurement that does not contain significant amounts of lines, as shown in Fig. (7.2).

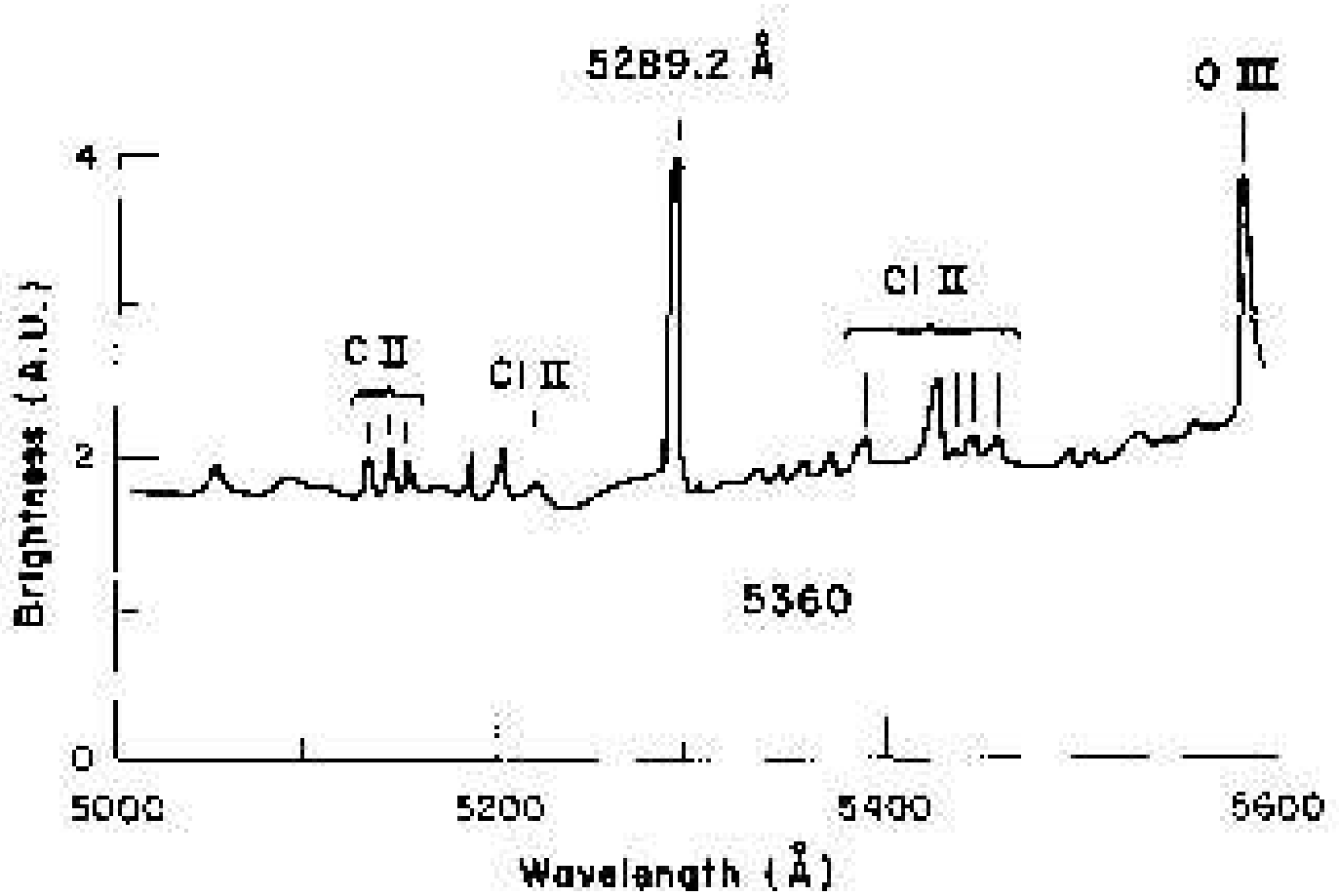

Figure 7.1: Trace of a spectrum in the region 5000-6000Å, with labelled line emissions, from Foord *et. al.* [17]. One must choose a portion of the continuum outside of significant line emission.

Shown in Fig. (7.2) and (7.3) is the experimental setup and Z_{eff} for several plasma configurations, given in [16].

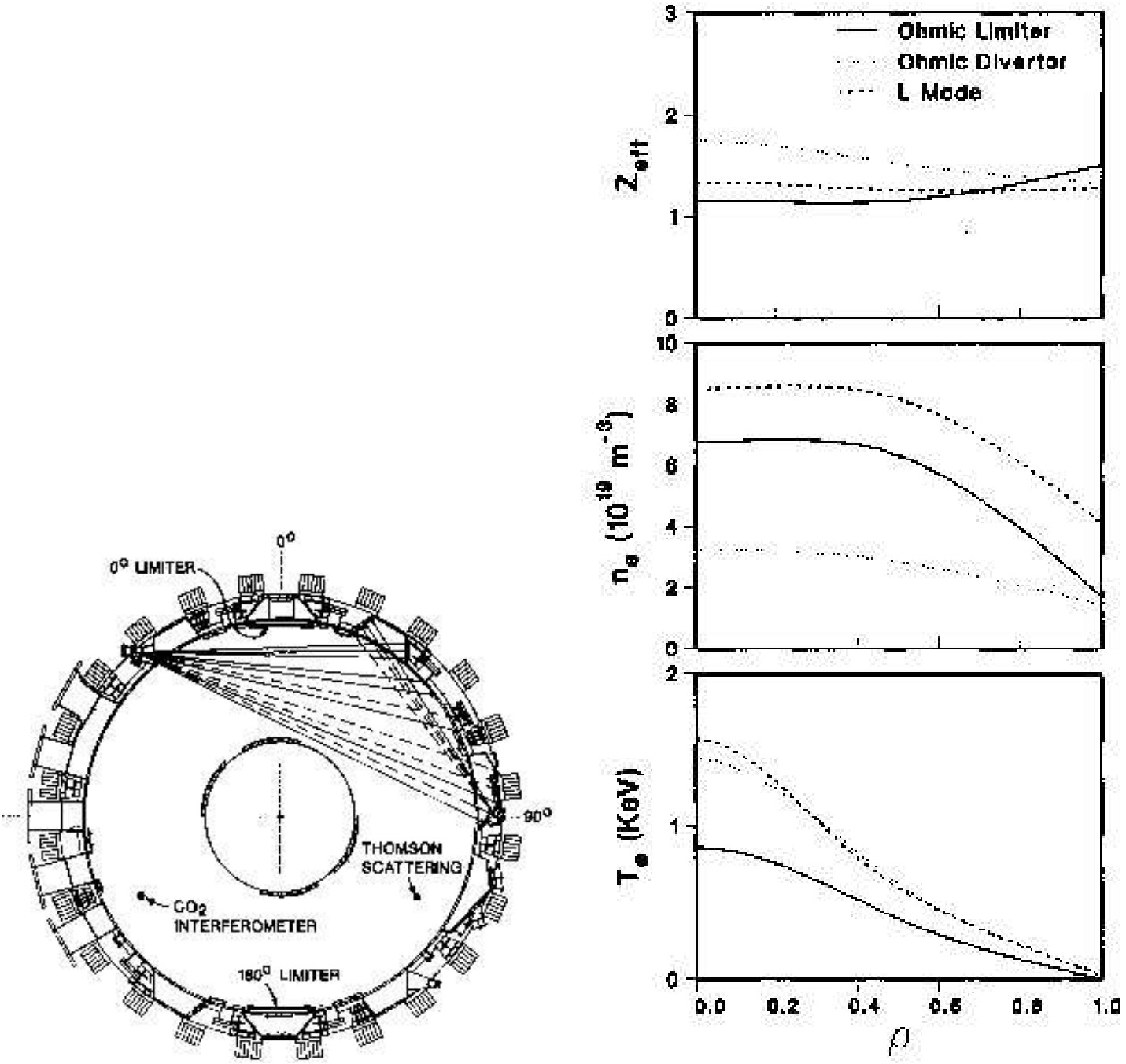

Figure 7.2: On left is the setup for the measurement of the visible bremsstrahlung measurement of Z_{eff}, averaging measurements of Z_{eff} across the different chords. Not shown here is the required measurement of T_e, which is performed through Thompson scattering measurements.

Figure 7.3: On the right are Z_{eff}, T_e, and n_e as a function of the enclosed toroidal flux – a coordinate directly related to the distance away from the magnetic axis of the noncircular DIII-D tokamak. This data was determined through Abel inversion of averaged quantities along the chords.

8 Measurements of Ion Temperature

Radiation measurements, whether from free charges or from incident microwaves or lasers, is dominated by electrons in the nonrelativistic environment of a toroidal fusion plasma. However, the fact that fusion devices produce neutrons allows one to determine the ion temperature from the spectrum of emitted neutrons. The first part of this section focuses on a quick summary of the theory of nuclear reactions in a fusion plasma, and the determination of ion temperature from the neutron spectrum. The second part focuses on a representative neutron spectrometer and neutron spectrum.

8.1 Neutron Energies from Nuclear Fusion Reactions

8.1.1 Relevant Reactions

The main fusion reactions in fusion devices are the following:

$$\mathrm{D} + \mathrm{T} \quad \rightarrow {}^{4}\mathrm{He}\,(3.5\ \mathrm{MeV}) + n\,(14.1\ \mathrm{MeV}) \tag{8.1}$$

$$\mathrm{D} + \mathrm{D} \quad \rightarrow_{50\%} \mathrm{T}\,(1.01\ \mathrm{MeV}) + p\,(3.02\ \mathrm{MeV}) \tag{8.2}$$

$$\rightarrow_{50\%} {}^{3}\mathrm{He}\,(0.82\ \mathrm{MeV}) + n\,(2.45\ \mathrm{MeV}) \tag{8.3}$$

$$\mathrm{T} + \mathrm{T} \quad \rightarrow {}^{4}\mathrm{He}\,(3.8\ \mathrm{MeV}) + 2n\,(7.6\ \mathrm{MeV}) \tag{8.4}$$

Where D refers to deuterium and T to tritium. A standard fit to the cross section to fusion, where E is the incident energy of the particles in keV and a barn (b) is 10^{-28} m^{-2}[18, 19], which arises from experimental fits to using the WKB approximation to model transmission rates across the Coulomb barrier (see, e.g., [20, 14]).

$$\sigma(E) = \frac{A_5 + \left[(A_4 - A_3 E)^2 + 1\right]^{-1} A_2}{E\left[\exp\left(A_1 E^{-1/2}\right) - 1\right]}\ \mathrm{b} \tag{8.5}$$

With the following *Duane coefficients* $A_1, \ldots A_5$ shown below: The reactivities between like particles (D-D or T-T) of a plasma, where n is the number density of the reacting species:

$$S = \frac{1}{2} n^2 \langle \sigma v \rangle \tag{8.6}$$

	D-D (8.2)	D-D (8.3)	D-T (8.1)	T-T (8.4)
A_1	46.097	47.88	45.95	38.39
A_2	372	482	50,200	448
A_3	4.36×10^{-4}	3.08×10^{-4}	1.368×10^{-2}	1.02×10^{-3}
A_4	1.220	1.177	1.076	2.09
A_5	0	0	409	0

And for unlike particles (such as D-T), where n_1 is the number density of species 1 and n_2 of species 2:

$$S = n_1 n_2 \langle \sigma v \rangle \tag{8.7}$$

And has dimensions $V^{-1}T^{-1}$, where V is a unit of volume and T is a unit of time. The quantity $\langle \sigma v \rangle$ is defined as the following:

$$n_1 n_2 \langle \sigma v \rangle = \int \sigma \left(|\mathbf{v}_1 - \mathbf{v}_2| \right) |\mathbf{v}_1 - \mathbf{v}_2| \, f_1 \left(\mathbf{v}_1 \right) f_2 \left(\mathbf{v}_2 \right) \, d^3\mathbf{v}_1 \, d^3\mathbf{v}_2 \tag{8.8}$$

Where f_1 and f_2 are normalized distribution functions, $\int f_i \left(\mathbf{v} \right) \, d^3\mathbf{v} = n_i$. The cross sections (in millibarns) and reactivities (in cm^3 s^{-1}) are given in Fig. (8.1).

8.1.2 Neutron Spectra from Nonrelativistic Collisions

Now take the case of deuteron-deuteron collisions that produce ^{3}He and a neutron of characteristic energies. Denote m_α and $\mathbf{u}_\alpha$ the mass and c.m. velocity of the He-3 nucleus, m_n and $\mathbf{u}_n$ the mass and c.m. velocity of the neutron, Q is the energy released by the reaction, and K is the relative kinetic energy of the interacting deuterons. Conservation of momentum and energy in the center of mass frame:

$$m_n \mathbf{u}_n + m_\alpha \mathbf{u}_\alpha = \mathbf{0} \tag{8.9}$$

$$Q + K = \frac{1}{2} m_n u_n^2 + \frac{1}{2} m_\alpha u_\alpha^2 = \frac{1}{2} m_n u_n^2 \left(1 + \frac{m_n}{m_\alpha} \right) \tag{8.10}$$

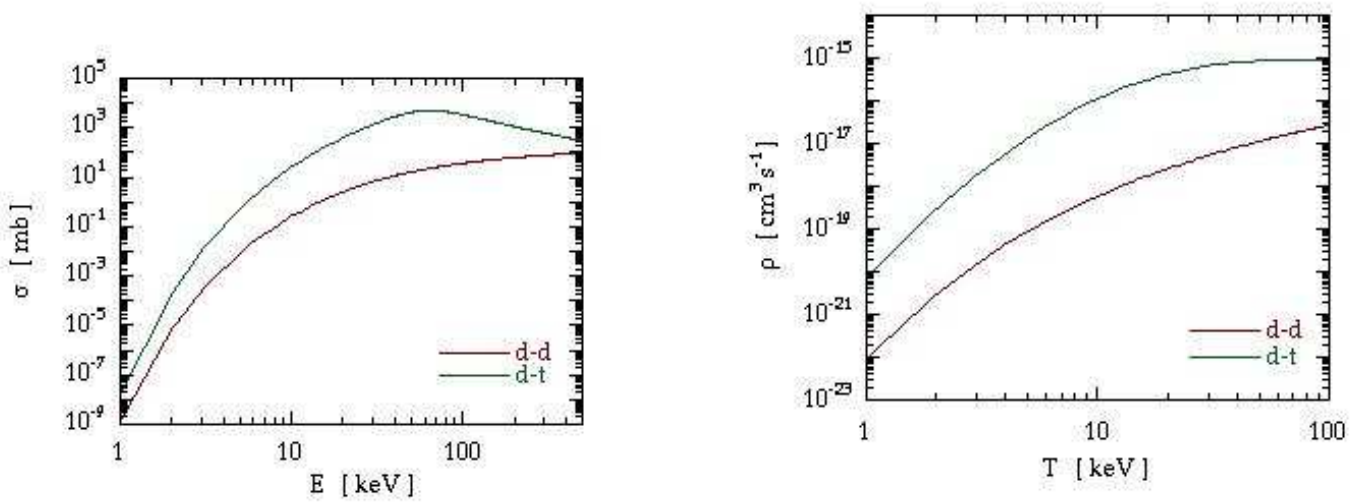

Figure 8.1: Cross sections (on left, in millibarns) and reactivities (on right, in $cm^3\ s^{-1}$) for a D-T plasma, as a function of ion temperature.

In the lab frame, the center-of-mass velocity of the two colliding deuterons is $\mathbf{V}$, so that the neutron's velocity in the lab frame $\mathbf{v}_n$ and its energy E_n:

$$\mathbf{v}_n = \mathbf{u}_n + \mathbf{V}$$
$$E_n = \frac{1}{2}m_n v_n^2 = \frac{1}{2}m_n u_n^2 + \frac{1}{2}m_n V^2 + m_n V u_n \cos\theta$$
$$E_n = \frac{1}{2}m_n V^2 + (Q+K)\frac{m_\alpha}{m_\alpha + m_n} + V\left(\frac{2m_n m_\alpha}{m_n + m_\alpha}(Q+K)\right)^{1/2}\cos\theta$$

Where θ is the angle between $\mathbf{u}_n$ and $\mathbf{V}$. One gets the following averaged energy of the neutrons emitted by this reaction, as well as the distribution of neutron energy about the average, for an isotropic distribution of reactants:

$$\overline{E_n} = \frac{1}{2}m_n\overline{V^2} + \frac{m_\alpha}{m_\alpha + m_n}\left(Q + \overline{K}\right)$$
$$\Delta E_n = E_n - \overline{E_n} = \frac{1}{2}m_n\left(V^2 - \overline{V^2}\right) + \frac{m_\alpha}{m_\alpha + m_n}\left(K - \overline{K}\right) +$$
$$\left(\frac{2m_\alpha m_n}{m_n + m_\alpha}(Q+K)\right)^{1/2}\cos\theta$$

For the case of nonrelativistic neutrons, with temperatures much smaller than the energy emitted by the reaction, $Q \gg T_i$, where $Q = 3.3$ MeV for the $\mathrm{D} + \mathrm{D} \rightarrow {}^3\mathrm{He} + n$ reaction:

$$E_n - \overline{E_n} \approx \left(\frac{2m_\alpha m_n Q}{m_n + m_\alpha}\right)^{1/2} V \cos\theta = \left(\frac{2m_\alpha m_n Q}{m_n + m_\alpha}\right)^{1/2} V_z \tag{8.11}$$

Thus, the distribution of $E_n - \overline{E}_n$ allows for a determination of the distribution of V, the center-of-mass velocity of the deuterons, along the direction of $\mathbf{u}_n \approx \mathbf{v}_n$ (again, since the thermal energy of the reactants is much smaller than the energy released by the reaction).

First, note that the rate of neutrons produced within some volume V_0 by the D-D reaction is given by the following:

$$\frac{dN_n}{dt} = \frac{1}{2} n_D^2 \langle \sigma v \rangle V_0$$

Where we assume some type of collimated detection system in which only neutrons within the volume V_0 are resolved. Furthermore, we resolve only neutrons with some energy E_n, so that the count rate per incident neutron energy:

$$\frac{\partial^2 N_n}{\partial t \partial E_n} = \frac{1}{2} V_0 \frac{\partial}{\partial E_n} \left(n_D^2 \langle \sigma v \rangle\right) \propto \frac{\partial}{\partial E_n} \left(n_D^2 \langle \sigma v \rangle\right)$$

However, for deuterium particles with Gaussian velocity distributions:

$$f_D = \frac{n_D}{(2\pi T/m_D)^{3/2}} \exp\left(-\frac{m_D v^2}{2T}\right)$$

And the reaction rate may be rewritten in terms of center-of-mass velocity $\mathbf{V} = \frac{1}{2}(\mathbf{v}_1 + \mathbf{v}_2)$ and relative

velocity $\mathbf{v} = \mathbf{v}_1 - \mathbf{v}_2$:

$$\begin{aligned}\langle \sigma v \rangle &= \int d^3\mathbf{V} \sigma(v) v f_D \left(\mathbf{V} + \frac{1}{2}\mathbf{v}\right) f_D \left(\mathbf{V} - \frac{1}{2}\mathbf{v}\right) d^3\mathbf{v} \\ &= \int \left(\frac{m_D}{\pi T}\right)^{3/2} \exp\left(-\frac{m_D V^2}{T}\right) d^3\mathbf{V} \times \\ &\int \sigma(v) v \left(\frac{m_D}{2\pi T}\right)^{3/2} \exp\left(-\frac{m_D v^2}{2T}\right) d^3\mathbf{v}\end{aligned} \tag{8.12}$$

And thus, we see that the number of neutrons observed, since $dE_n \propto dV_z$:

$$\frac{\partial^2 N_n}{\partial t \partial E_n} \propto \exp\left(-\frac{m_D V_z^2}{T}\right) \int \sigma(v) v \left(\frac{m_D}{2\pi T}\right)^{3/2} \exp\left(-\frac{m_D v^2}{2T}\right) d^3\mathbf{v}$$

And so the observed neutron energy spectrum for this reaction:

$$\begin{aligned}P\left(E_n\right) &\propto \exp\left(-\frac{M V_z^2}{2T}\right) = \exp\left(-\frac{m_D \left(E_n - \overline{E_n}\right)^2}{\frac{2m_\alpha m_n}{m_\alpha + m_n} QT}\right) \\ P\left(E_n\right) &\propto \exp\left(-\frac{\left(E_n - \overline{E_n}\right)^2}{2QT\left(m_\alpha/m_D\right)\left(m_n/m_D\right)}\right)\end{aligned} \tag{8.13}$$

However, problems arise due to the fact that the reaction rate is dominated by particles at the tail of the thermal distributions, from neutron spectral contamination from molybdenum walls in some tokamaks, and from neutrons reflected and scattered by the metallic structures in a tokamak. Generally, for 14.1 MeV emission, the signal from fusion neutrons is much larger than that of the background noise – the energy width gives the ion temperature in the plasma. For 2.45 and 3.02 MeV emission, the profile of the peaks must be reconstructed because the signal from fusion neutrons is much smaller than the background level.

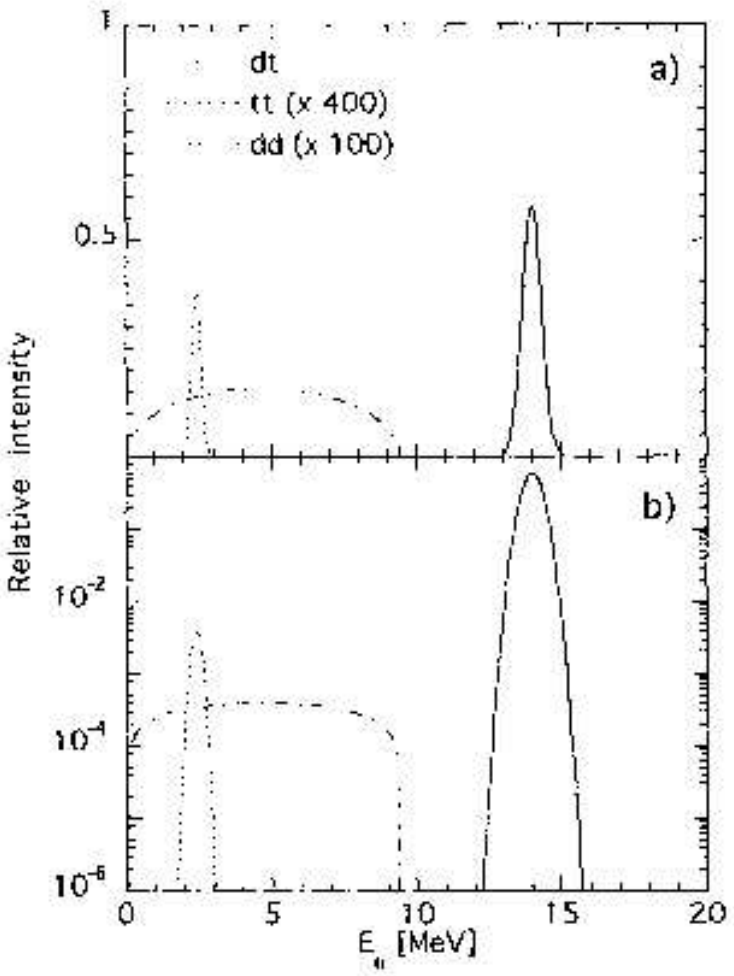

Fig. 4. The neutron emission spectrum of the deuterium–tritium (of equal abundance) plasma calculated for the ion temperature of 20 keV. The three contributions are due to d + t -> α + n, d + d -> ^{3}He + n and t + t -> α − 2n. The peak width reflects the Doppler broadening and the relative intensities the reactivity ratios at 20 keV: linear scale in (a) and logarithmic in (b).

Figure 8.2: Shown here is neutron spectrum within a DT plasma with temperature $T_i = 20$ keV. The neutron spectrum peak centered about 14.1 MeV is due to $\mathrm{D} + \mathrm{T} \rightarrow {}^4\mathrm{He} + n$, while the peak at 2.5 MeV is due to $\mathrm{D} + \mathrm{D} \rightarrow {}^3\mathrm{He} + n$. The broad component is due to three-body interactions $\mathrm{T} + \mathrm{T} \rightarrow {}^4\mathrm{He} + 2n$. This diagram is taken from [21].

8.1.3 Complications Arising In Neutron Spectral Measurements

There are several important sources of uncertainty and neutron spectral noise in determining ion temperature. First, for a deuterium plasma, n_D must be determined if a temperature measurement is made from a total neutron count; in plasmas with low $Z_{\text{eff}} < 2$, $n_D \sim n_e$. However, since the temperature depends more strongly on ion temperature, this is generally not a problem in fusion plasmas.

Sources of nonfusion neutrons may be through runaway electrons that interact with protons, $n + e \rightarrow p + \bar{\nu}_e$. This may be an especially strong source of nonfusion neutrons in RF-heated plasmas, such as Alcator. A second source is through the disintegration of deuterons, which have a binding energy of 2.2 MeV,

through electron interactions or through photodisintegration. A third, and particularly significant, source of additional neutrons arise from the wall itself, which itself may be activated and emit neutrons. A notable example consists of activated molybdenum at the walls, which emit neutrons via the following processes:

$$\begin{aligned} {}^{97}\mathrm{Mo} + e &\rightarrow {}^{96}\mathrm{Mo} + e + n \\ {}^{97}\mathrm{Mo} + \gamma &\rightarrow {}^{98}\mathrm{Mo} + n \end{aligned} \tag{8.14}$$

Other effects can distort the observed spectrum of fusion neutrons. RF-heating of the ions and the injection of neutral beams of a specific energy can shift the location of the peaks; reactions, such as $\mathrm{D} + \mathrm{D} \rightarrow \mathrm{T} + p$, and collisions between the reactants can lead to Doppler broadening of the peaks. However, the Doppler broadening results in a change in the width of the peaks of order T_i; the peak itself is already of width $\sqrt{QT_i} \gg T_i$, so Doppler broadening is not an important effect in most fusion plasmas. Furthermore, neutral-beam injection and RF-heating shifts the peaks by a predictable energy.

Shown in Fig. (8.3) and (8.4) below are representative neutron spectra within a tokamak.

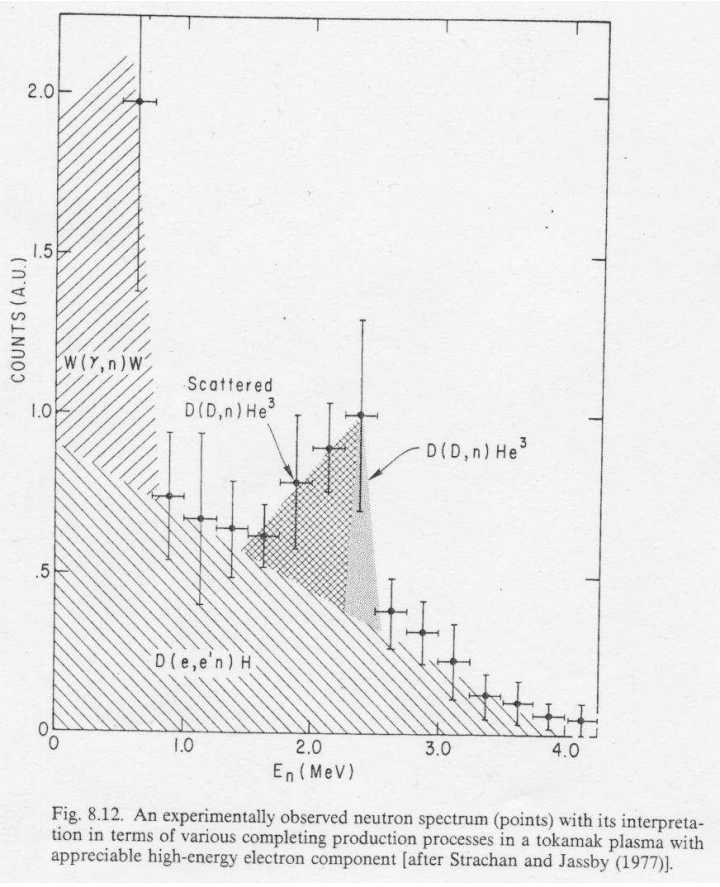

Fig. 8.12. An experimentally observed neutron spectrum (points) with its interpretation in terms of various completing production processes in a tokamak plasma with appreciable high-energy electron component [after Strachan and Jassby (1977)].

Figure 8.3: Plot of neutron spectrum from a tokamak plasma showing various sources of nonfusion neutrons: 1) neutron emission from the walls $W + \gamma \rightarrow n + W$, where W refers to molybdenum or other activated nucleus; 2) deuterium disintegration $\mathrm{D} + e \rightarrow e + n + \mathrm{H}$; 3) neutrons from the process $\mathrm{D} + n \rightarrow {}^3\mathrm{He} + n$ that are scattered by solid structures in the tokamak; and 4) superimposed over the large background, the fusion neutrons from the thermal fusion plasma and from the process $\mathrm{D} + n \rightarrow {}^3\mathrm{He} + n$. This above plot is taken from [22], and the figure copied from [2].

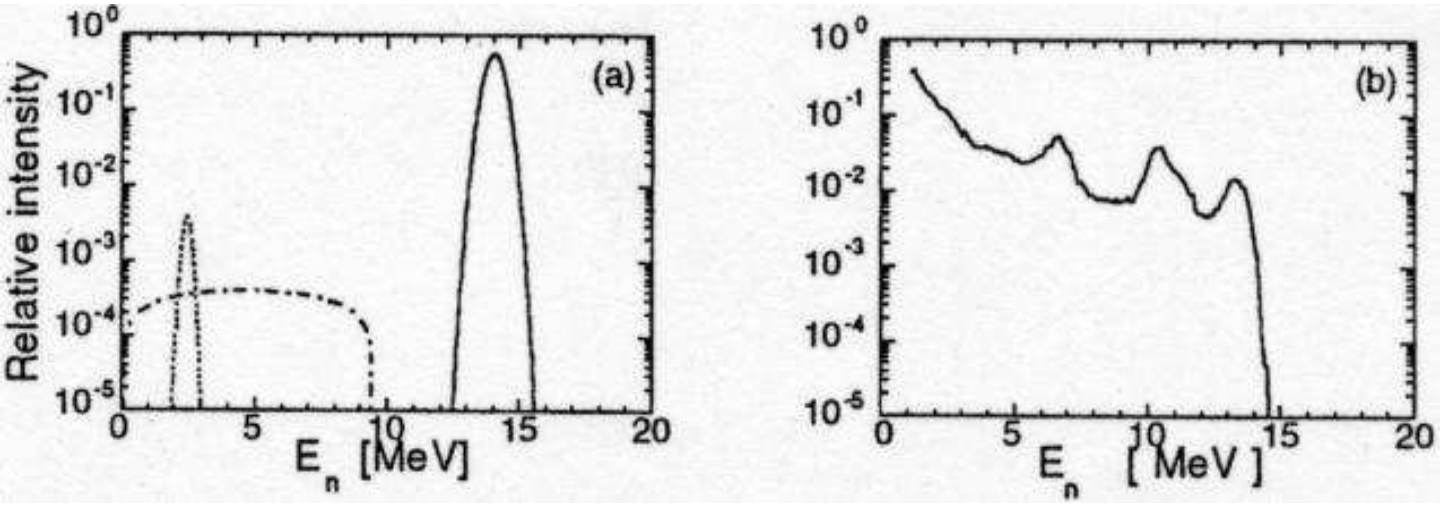

Figure 8.4: On left is the normalized neutron spectrum seen from neutrons in a 20 keV D-T plasma in a tokamak. On right is the spectrum from the plasma facing wall in the tokamak. These plots are taken from [23]. Note that the 14.1 MeV neutron spectrum can be directly resolved, since the background is relatively low at these energies, while the 2.5 MeV neuton spectrum can be discriminated against.

8.2 Experimental Setup for Ion Temperature Measurement

Neutron emission from fusion processes is dominated by the highest-temperature region of the plasma – hence the measurement of ion temperature by neutron emission gives one a good estimate of the central plasma ion temperature in a tokamak. Second, measurements along multiple chords of the neutron spectrum are then Abel-inverted to determine the ion temperature profiles in space and time.

Shown in Fig. (8.5) is a setup of neutron detection in a tokamak.

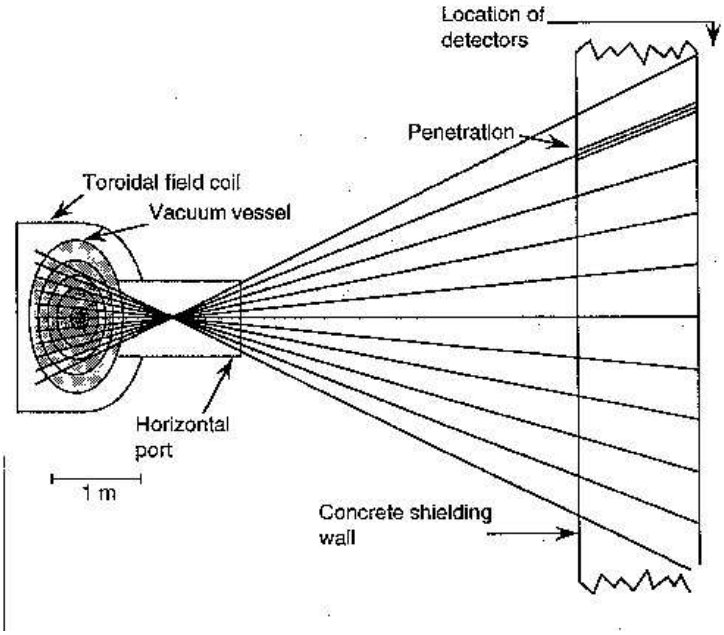

Figure 8.5: Plot of the neutron detector setup. Detectors are placed at various locations in order to measure the chord-averaged neutron spectrum. The input flux of neutrons to each detector is collimated, with a concrete barrier, in order to minimize other sources of neutrons (scattered neutrons, wall neutrons) as much as possible. This plot is taken from[24].

With a proton recoil detector used in measuring the neutron spectrum.

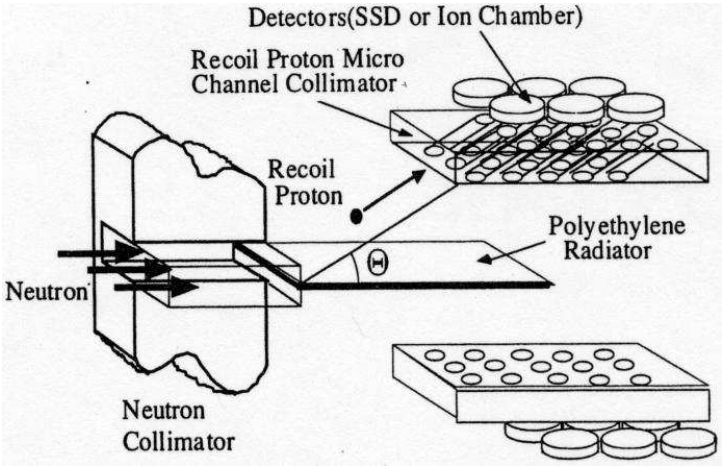

Figure 8.6: Typical detector used to measure the incoming neutron spectrum. A neutron ejects and scatters a proton from a polyethylne plastic film and detected by a silicon diode (SSD) or an ion chamber. This schematic is taken from [25]. Typical neutron detectors measuring the ion temperature have spatial resolutions of 30 cm, time resolution of 100 ms, and accuracy of 10% in an ion temperature measurement.

Neutron spectrum resolution is an important factor in resolving the fusion neutron spectrum, and hence the ion temperature, as well as discriminating the fusion neutrons from other neutron sources: And shown in Fig. (8.8) is the issue of resolving the 2.5 MeV neutron peak from the wall neutron emission.

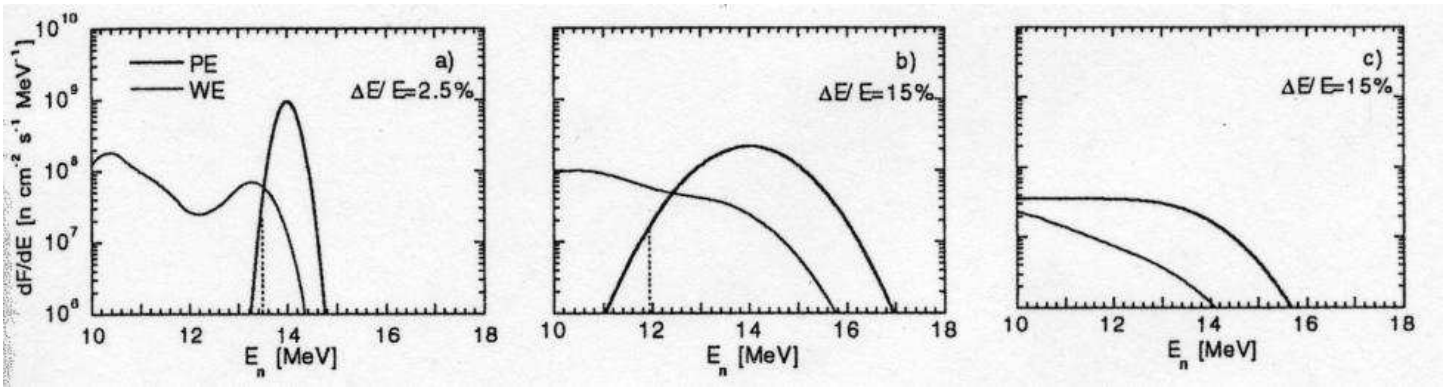

Figure 8.7: wall emission (WE) and 14.1 MeV neutron spectrum (PE) from a D-T plasma at 20 keV, with various neutron energy resolutions of a detector. This is taken from [23].

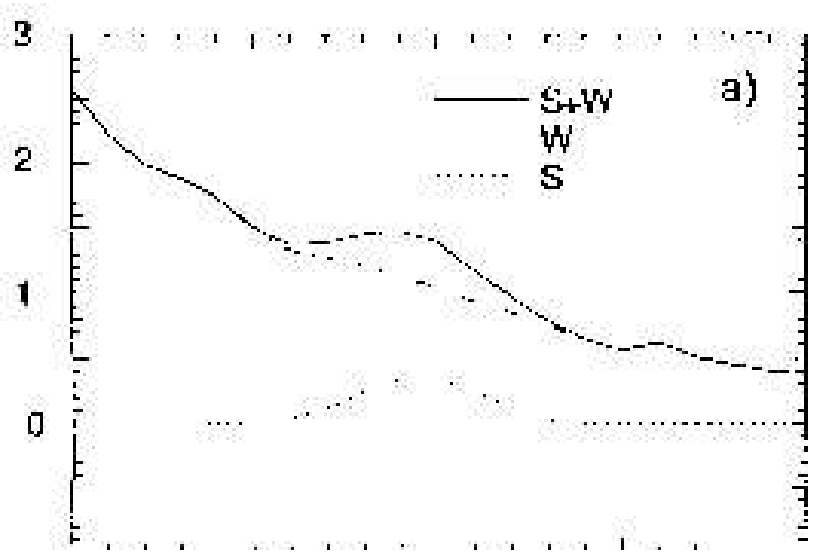

Figure 8.8: The difficulty in resolving the 2.5 MeV peak from the wall emission, in a 20 keV D-T tokamak plasma. Neutron spectral intensity is given in units of 10^9 n cm^{-2} s^{-1} MeV^{-1} and energy (on horizontal axis) ranges from 1.5 MeV on the right to 3.5 MeV on left with equal energy spacing. Taken from [21].

9 Summary of Diagnostic Methods

This report discussed diagnostic methods that measure electron temperature, electron density, magnetic fields (either through direct or indirect measurements), ion temperature, and the impurity level within the plasma, through measurements of Z_{eff}.

These methods are used, for example, to characterize the equilibrium magnetic field. Magnetic field measurements along the plasma edge can measure the magnetic field and its derivative at the boundary of the plasma. Measurements of the internal magnetic field, through Faraday rotation, as well as global magnetic measurements (such as magnetic pressure through diamagnetic coils, poloidal flux through saddle coils, and the toroidal current through Rogowski coils) can allow one to determine the current profile within the plasma. Measurements of temperature and density profiles within the plasma (through ECE, reflectometry, and interferometry) is also used to get a pressure profile. These measurements of magnetic field at a boundary, and current and pressure within the plasma can allow one to reconstruct the equilibrium magnetic field and pressure in a force-free MHD configuration (see, e.g., [26]).

Other diagnostics, such as the Langmuir probe measurements of density and temperature, were not discussed. Langmuir probes, for example, can only measure particle fluxes and species temperatures towards the plasma edge. Line measurements were also not discussed here; measurements of the Doppler broadening of emission lines can allow for an independent determination of the local pressure, and plasma rotation is seen through Doppler-shifted emission of iron lines. A full set of diagnostics in a tokamak[27], including those not discussed in this report, are shown in the Tab. (9.1), with their spatial and temporal resolutions.

Table 9.1: Ignitor Diagnostics

Plasma parameter	Diagnostic	Measured quantities	Δx, Δt	Instrument
Current, Voltage	MME	I_p, V_{loop}	1 ms	Rogowski coils, external loops
Position, Shape	MMI	B_{pol}, B_ϕ	1 ms	Internal loops, saddle loops
MHD β	MMI	B	> 1 μs	diamagnetic loops, pick-up coils
Electron Temperature	ECE	$T_e(r)$	3 cm, 5 ms	Michelson polychromator
	Thompson Scattering	$T_e(r)$, $n_e(r)$	3 cm, 5 μs	Nd laser
Ion Temperature	CCS	T_i, T_e, n_Z, v_ϕ	3 cm, 50 ms	Curved crystal spectrometer
	Neutron Spectrometer	$T_i(r)$, n_D, n_T	6 cm, 50 ms	proton recoil + time-of-flight
Density	Interferometry, Reflectometry	$n_e(r)$, $\overline{n_e}$		CO_2 interferometry, Faraday rotation, microwave reflectometer
Radiated Power	Bolometry		3 cm, 1-100 ms	Metal resistor
Impurity	Visible Spectroscopy			
Z_{eff}	Visible Bremsstrahlung			
Current Profile	Polarimeter			Faraday rotation
Neutrons	Counters, Foil Activation	neutron dosage		

Furthermore, many of the above sets of diagnostics allow for separate, independent measurements of plasma parameters – this is useful, in that most measurements are effective only over a finite range of plasma parameters, hence over a finite range in space and time within the tokamak plasma. However, a discussion of diagnostic methods beyond those within this report was not made for the following reasons: 1) it is typically not used in the high temperature regimes of tokamaks (i.e. Langmuir probes); or 2) the additional techniques (such as visible spectroscopy and bolometry) are discussed in greater detail and have extensive applications outside plasma physics – in astronomy, space physics, nuclear physics, or particle physics.

10 Acknowledgements

I wish to thank Dr. Francesca Bombarda for very useful advice on plasma diagnostic techniques – in giving a summary of plasma techniques and in recommending a seminal reference[2] – without which I would not have been able to decipher much of the literature on plasma diagnostic techniques.

References

[1] J. Sheffield, *Plasma Scattering of Electromagnetic Radiation* (Academic Press, New York, 1975).

[2] I. H. Hutchinson, *Principles of Plasma Diagnostics* (Academic Press, New York, 1987).

[3] R. H. Huddlestone and S. L. Leonard, eds., *Plasma Diagnostic Techniques* (Academic Press, New York, 1965).

[4] M. A. Heald and C. B. Wharton, eds., *Plasma Diagnostic Techniques With Microwaves* (Wiley, New York, 1965).

[5] P. E. Stott et. al., ed., *Diagnostics for Experimental Thermonuclear Fusion Reactors* (Plenum Press, New York, 1996).

[6] F. F. Chen, *Introduction to Plasma Physics* (Plenum Press, New York, 1965).

[7] F. Alladio and P. Micozzi, *Magnetic diagnostics*, URL `http://www.frascati.enea.it/ignitor/default/engineering/ME.pdf`.

[8] I. H. Hutchinson, Plasma Phys. & Controlled Fusion **18**, 246 (1976).

[9] J. H. Irby et. al., Rev. Sci. Inst. **59**, 1568 (1988).

[10] M. O'Gorman, Rev. Sci. Inst. **72**, 1063 (2001).

[11] V. L. Ginzburg, *Propagation of Electromagnetic Waves in Plasma* (Gordon and Breach, New York, 1961).

[12] L. D. Landau and E. M. Lifshitz, *Quantum Mechanics: Nonrelativistic Theory* (Addison-Wesley, Reading, MA, 1951).

[13] E. de la Sanchez et. al., Rev. Sci. Inst. **66**, 403 (1995).

[14] B. Carroll and D. Ostlie, *An Introduction to Modern Astrophysics* (Addison-Wesley, New York, 1996).

[15] D. Johnson et. al., Rev. Sci. Inst. **56**, 1015 (1985).

[16] D. P. Schissel et. al., Phys. Fluids **31**, 3738 (1988).

[17] M. S. Foord et. al., Rev. Sci. Inst. **53**, 1407 (1982).

[18] G. H. Miley et. al., Tech. Rep. COO-2218-17, University of Illinois, Urbana, IL (1974).

[19] B. H. Duane, Tech. Rep. BNWL-1685, Brookhaven National Laboratory (1972).

[20] G. Gamow and C. Critchfield, *Theory of the Atomic Nucleus and Nuclear Energy Sources* (Oxford University Press, London, 1949).

[21] P. Antozzi et. al., Nucl. Instr. & Meth. A **368**, 457 (1996).

[22] J. D. Strachan and D. L. Jassby, Proc. Am. Nuc. Soc. (1976).

[23] J. Källne and the NPF Collaboration, *Diagnostics for Experimental Thermonuclear Fusion Reactors* (Plenum Press, New York, 1996), chap. Neutron Spectrometry for ITER.

[24] F. Bombarda, *Ignitor diagnostics* (2002), URL `http://www.ppl.gov/snowmass_2002/monday_july15/mfe_bombarda.pdf`.

[25] T. Nishitani et. al., *Diagnostics for Experimental Thermonuclear Fusion Reactors* (Plenum Press, New York, 1996), chap. Neutron Spectrometers for ITER.

[26] E. Lazarro, *Diagnostics for Experimental Thermonuclear Fusion Reactors* (Plenum Press, New York, 1996), chap. Magnetic Equilibrium Reconstruction Techniques for Tokamak Reactors.

[27] *Ignitor diagnostics*, URL `http://www.frascati.enea.it/ignitor/default/engineering/Ignitor_Diagnostics.htm`.